
Improving the Euclidean Diffusion Generation of Manifold Data by Mitigating Score Function Singularity

Zichen Liu ^a, Wei Zhang ^{*b}, and Tiejun Li ^{*a,c,d}

^aCenter for Data Science, Peking University

^bZuse Institute Berlin

^cSchool of Mathematical Sciences, Peking University

^dCenter for Machine Learning Research, Peking University

Abstract

Euclidean diffusion models have achieved remarkable success in generative modeling across diverse domains, and they have been extended to manifold case in recent advances. Instead of explicitly utilizing the structure of special manifolds as studied in previous works, we investigate direct sampling of the Euclidean diffusion models for general manifold-constrained data in this paper. We reveal the multiscale singularity of the score function in the embedded space of manifold, which hinders the accuracy of diffusion-generated samples. We then present an elaborate theoretical analysis of the singularity structure of the score function by separating it along the tangential and normal directions of the manifold. To mitigate the singularity and improve the sampling accuracy, we propose two novel methods: (1) Niso-DM, which introduces non-isotropic noise along the normal direction to reduce scale discrepancies, and (2) Tango-DM, which trains only the tangential component of the score function using a tangential-only loss function. Numerical experiments demonstrate that our methods achieve superior performance on distributions over various manifolds with complex geometries.

1 Introduction

Recent advances in diffusion models [9, 28, 29, 31] have demonstrated remarkable success in generative modeling in various domains, including image generation [10], audio synthesis [3], molecule generation [11], and other applications [16, 36]. These models operate through a forward process, which gradually perturbs data into noise, and a reverse process, which reconstructs the data from noise.

Beyond Euclidean space, many scientific fields involve data distributions constrained to Riemannian manifolds. Examples include geographical sciences [22] using spheres, protein structures [34] and robotic movements [27] with $SE(3)$ and $SO(3)$, lattice quantum chromodynamics [20] with $SU(3)$, 3D computer graphics [12] with triangular meshes, and cell development [15] with the Poincaré disk. To model such data, recent works [7, 13, 20, 37] have extended diffusion models to Riemannian manifolds, achieving notable progress by leveraging manifold geometry and curvature information. Nonetheless, these methods face challenges due to the cost of simulating diffusion and obtaining accurate geometric information like the heat kernel.

*Corresponding author: tieli@pku.edu.cn (T. Li), wei.zhang@fu-berlin.de (W. Zhang)

On the other hand, a natural idea is to directly apply diffusion models designed for Euclidean space to manifold-structured data. However, this approach encounters a fundamental challenge: the singularity of the score function. Prior studies under the manifold hypothesis [6, 21, 23] have identified that in the reverse process, the norm of the score function grows explosively. Recent works [2, 21, 23] have theoretically analyzed this singularity under the Ornstein-Uhlenbeck process, providing asymptotic bounds on the score function and introducing structural assumptions on the data distribution. In this paper, we further enhance these insights and propose methods for mitigating the singularity of the score function in the Euclidean space.

Our work. We consider a probability distribution on a known d -dimensional submanifold \mathcal{M} embedded in \mathbb{R}^n . Given samples from this distribution, our objective is to generate new samples by directly applying Euclidean diffusion models. First, under the Variance Exploding Stochastic Differential Equations (VESDE) framework with such a manifold setting, we theoretically demonstrate that the perturbed score function exhibits distinct scales along the tangential and normal components. To address this issue, we propose the following two methods to improve diffusion models (DM):

1. **Niso-DM:** Perturbs data with non-isotropic noise by introducing additional noise along the normal direction during the forward diffusion process. This reduces the scale discrepancy between the tangential and normal directions, making the relaxed score function easier to approximate.
2. **Tango-DM:** Trains only the tangential component of the score function using a tangential-only loss function. By skipping the training of the normal component, this method avoids the learning difficulties caused by the multiscale issue.

Our main contributions are as follows:

- We present an elaborate theoretical analysis of the multiscale singularity structure of the score function by separating it along the tangential and normal directions of the manifold in the embedded Euclidean space. Furthermore, we investigate the relationship between the full-space score function and the original Riemannian score function, which has not been considered before.
- We propose two novel methods, Niso-DM and Tango-DM, making the relaxed score function easier to approximate. We also give theoretical analysis of the Niso-DM. Empirically, our methods demonstrate superior performance on distributions across various complex and non-trivial manifolds. This is in sharp contrast with previous methods which can only handle special manifolds with particular analytical structure.

2 Backgrounds and preliminaries

2.1 Diffusion models

Diffusion models can be formulated using stochastic differential equations (SDEs). Specifically, data perturbation is modeled by the following forward SDE:

$$dX_t = f(X_t, t)dt + g(t)dW_t, \quad (1)$$

where f and g are fixed drift and diffusion coefficients, respectively. The time-dependent distribution p_t , driven by the stochastic process X_t , converges to a limiting distribution $\mathcal{N}(0, \sigma_T^2 I)$ as $t \rightarrow +\infty$. By carefully selecting f and g , this distribution can be approximated as $p_T \approx \mathcal{N}(0, \sigma_T^2 I)$. The corresponding reverse-time SDE, which transports p_T back to the initial probability density function (pdf) p_0 , is given by:

$$dX_t = (f(X_t, t) - g(t)^2 \nabla_x \log p_t(X_t)) dt + g(t)d\bar{W}_t, \quad (2)$$

where \bar{W}_t is a standard Brownian motion in reverse time.

Inspired by this formulation, diffusion models employ a neural network $s_\theta(x, t)$ to approximate the score function $\nabla_x \log p_t(x)$. Since $p_t(x)$ is analytically unknown, direct optimization of the quadratic loss:

$$\mathcal{L}_{\text{quad}}(\theta) = \mathbb{E}_{t \sim \mathcal{U}(0,1)} \lambda_t \ell_{\text{quad}}(t, \theta), \quad (3)$$

$$\ell_{\text{quad}}(t, \theta) = \mathbb{E}_{x_t \sim p_t} \|s_\theta(x_t, t) - \nabla_{x_t} \log p_t(x_t)\|^2, \quad (4)$$

is intractable. Instead, score matching techniques such as denoising score matching [33] are commonly used, formulated as:

$$\ell_{\text{dsm}}(t, \theta) = \mathbb{E}_{x, x_t} \|s_\theta(x_t, t) - \nabla_{x_t} \log p_t(x_t|x)\|^2. \quad (5)$$

To utilize the above loss, the computability of $p_t(x_t|x)$ requires specific SDEs, such as the following VPSDE and VESDE introduced by [31].

1. Variance Preserving SDE (VPSDE):

$$dX_t = \frac{1}{2}\beta(t)X_t dt + \sqrt{\beta(t)}dW_t. \quad (6)$$

2. Variance Exploding SDE (VESDE):

$$dX_t = \sqrt{\frac{d\sigma_t^2}{dt}}dW_t, \quad (7)$$

where σ_t is a predefined noise scale, which is commonly chosen as $\sigma_t = \sigma_{\min}(\sigma_{\max}/\sigma_{\min})^{t/T}$. In this case, $p_t(x_t|x)$ follows a Gaussian distribution: $\mathcal{N}(x_t|x, \sigma_t^2 I)$.

Choice of SDE in this work. In this study, we choose VESDE for its advantageous properties. Under VESDE, the mean of the perturbed distribution remains unchanged, preserving the original manifold structure. At any time, the perturbed distribution $p_t(x)$ can be viewed as points on the original manifold \mathcal{M} with added noise. This simplifies theoretical analysis and avoids the complications introduced by the evolving manifold in VPSDE. In fact, VPSDE involves an evolving manifold over time, defined as $\mathcal{M}_t = \{e^{-\frac{1}{2}\int_0^t \beta(s)ds}x \mid x \in \mathcal{M}\}$ as the mean with noise perturbation.

2.2 Riemannian manifolds and notation

In this paper, the manifold \mathcal{M} is viewed as $\mathcal{M} = \{x \in \mathbb{R}^n \mid \xi(x) = 0\}$ embedded in \mathbb{R}^n , $\xi : \mathbb{R}^n \rightarrow \mathbb{R}^{n-d}$ is a known function, and we assume that $\nabla \xi(x) \in \mathbb{R}^{n \times (n-d)}$ has always full column rank. The target distribution is formulated as $p_0(x)d\sigma_{\mathcal{M}}(x)$, where $p_0(x)$ is an unknown density and $d\sigma_{\mathcal{M}}(x)$ represents the volume form of \mathcal{M} . The unit normal vector at a point $x \in \mathcal{M}$ is given by $N(x) = \nabla \xi(x) (\nabla \xi(x)^T \nabla \xi(x))^{-\frac{1}{2}}$. For $x \in \mathcal{M}$, the Riemannian score function is defined as $\nabla_x^{\mathcal{M}} \log p_0(x) = P(x) \nabla_x \log p_0(x)$, where $P(x)$ is the projection matrix onto the tangent space of \mathcal{M} . The projection matrix $P(x)$ is computed as

$$P(x) = I - N(x)N(x)^T = I - \nabla \xi(x) (\nabla \xi(x)^T \nabla \xi(x))^{-1} \nabla \xi(x)^T. \quad (8)$$

3 Scale discrepancy of score functions

It is commonly understood that singularities arise when Euclidean diffusion models are directly applied to data with manifold structures. In this section, we examine the singularity of diffusion models under VESDE, following the settings in Section 2.2. By introducing Gaussian noise across the entire space, the perturbed data become distributed throughout \mathbb{R}^n , deviating from their original confinement to the d -dimensional submanifold \mathcal{M} . The perturbed distribution is given by

$$p_\sigma(\tilde{x}) = \int_{\mathcal{M}} p_0(x) p_\sigma(\tilde{x}|x) d\sigma_{\mathcal{M}}(x) = \int_{\mathcal{M}} p_0(x) (2\pi\sigma^2)^{-\frac{n}{2}} e^{-\frac{|x-\tilde{x}|^2}{2\sigma^2}} d\sigma_{\mathcal{M}}(x), \quad (9)$$

where \tilde{x} is a variable in the embedded space \mathbb{R}^n , $p_\sigma(\tilde{x}|x)$ denotes the isotropic perturbation pdf $\mathcal{N}(x, \sigma^2 I)$, $p_\sigma(\tilde{x})$ is the perturbed pdf defined on \mathbb{R}^n , and $p_0(x)$ is only defined on \mathcal{M} . Hereafter, the subscript of p denotes the noise scale σ instead of the time t .

When the noise scale σ is small, the perturbed distribution becomes tightly concentrated around its mean, resulting in a steep gradient landscape for $-\log p_\sigma(\tilde{x})$. As σ approaches zero, this steepness appears as sharp variations and introduces multiscale challenges. In Theorem 3.1, we provide a rigorous and refined results on this singularity compared to previous works. Eq. (10) shows that the score function explodes entirely due to the normal direction to the manifold, represented by $x^* - \tilde{x}$.

After subtracting this term, the remaining components are of order $O(1)$. Furthermore, Equations (11) and (12) establish a novel connection between the Riemannian score function and the score perturbed function in the ambient space for points on the manifold, which has not been considered in previous works. The proof is provided in Appendix A.

Theorem 3.1. *Let $P(x) \in \mathbb{R}^{n \times n}$ denote the projection matrix at $x \in \mathcal{M}$. Assume that $\mathbb{E}_{p_0} \|x\| < +\infty$ and $M_1 = \sup_{x \in \mathcal{M}} \max_{1 \leq i, j, j' \leq n} \left| \frac{\partial P_{ij}}{\partial x_{j'}}(x) \right| < +\infty$. The following two asymptotic expansions for $p_\sigma(\tilde{x})$ defined in (9) hold:*

1. For $\tilde{x} \notin \mathcal{M}$, assume that $x^* \in \mathcal{M}$ is the unique minimizer of $\min_{x \in \mathcal{M}} \|x - \tilde{x}\|$, and that $\|x^* - \tilde{x}\|_\infty < \frac{1}{n^2 M_1}$. Under these conditions, as $\sigma \rightarrow 0$, we have

$$\nabla_{\tilde{x}} \log p_\sigma(\tilde{x}) = \frac{x^* - \tilde{x}}{\sigma^2} + O(1). \quad (10)$$

2. For $\tilde{x} \in \mathcal{M}$, as $\sigma \rightarrow 0$, we have

$$\nabla_{\tilde{x}} \log p_\sigma(\tilde{x}) = \nabla_{\tilde{x}}^{\mathcal{M}} \log p_0(\tilde{x}) - \frac{1}{2} \sum_{j, j'=1}^n \frac{\partial P_{ij}}{\partial x_{j'}}(\tilde{x}) P_{jj'}(\tilde{x}) + O(\sigma), \quad (11)$$

$$\nabla_{\tilde{x}}^{\mathcal{M}} \log p_\sigma(\tilde{x}) = \nabla_{\tilde{x}}^{\mathcal{M}} \log p_0(\tilde{x}) + O(\sigma). \quad (12)$$

Next, based on Theorem 3.1, we analyze the scale discrepancy of the score function between its tangential and normal components. To achieve this, we first extend the projection matrix P from \mathcal{M} to the entire space \mathbb{R}^n continuously. A natural extension is to define P in the same manner as in (8), assuming that ξ is well-defined and smooth on \mathbb{R}^n . With this extended projection matrix, we further define the tangential and normal components of the score function for any $\tilde{x} \in \mathbb{R}^n$ as $P(\tilde{x}) \nabla_{\tilde{x}} \log p_\sigma(\tilde{x})$ and $P^\perp(\tilde{x}) \nabla_{\tilde{x}} \log p_\sigma(\tilde{x})$, respectively, where we denote $P^\perp(\tilde{x}) = I - P(\tilde{x})$. Using this extended definition, we then decompose the quadratic loss ℓ_{quad} into two parts: $\ell_{\text{quad}}^\parallel$ and ℓ_{quad}^\perp , corresponding to the tangential and normal components, respectively.

$$\begin{aligned} \ell_{\text{quad}} &= \mathbb{E}_{\tilde{x} \sim p_\sigma(\tilde{x})} \|s_\theta(\tilde{x}, t) - \nabla_{\tilde{x}} \log p_\sigma(\tilde{x})\|^2 \\ &= \mathbb{E}_{\tilde{x} \sim p_\sigma(\tilde{x})} \|P(\tilde{x}) s_\theta(\tilde{x}, t) - P(\tilde{x}) \nabla_{\tilde{x}} \log p_\sigma(\tilde{x})\|^2 \\ &\quad + \mathbb{E}_{\tilde{x} \sim p_\sigma(\tilde{x})} \|P^\perp(\tilde{x}) s_\theta(\tilde{x}, t) - P^\perp(\tilde{x}) \nabla_{\tilde{x}} \log p_\sigma(\tilde{x})\|^2 \\ &=: \ell_{\text{quad}}^\parallel + \ell_{\text{quad}}^\perp. \end{aligned} \quad (13)$$

Using Eq. (10) and the facts that $P(x^*)(x^* - \tilde{x}) = 0$, $P(\tilde{x}) = P(x^*) + O(\tilde{x} - x^*)$ and $\mathbb{E}_{\tilde{x}|x}(x^* - \tilde{x}) = O(\sigma)$, where $\mathbb{E}_{\tilde{x}|x}$ denotes the expectation with respect to $p_\sigma(\tilde{x}|x)$, the two terms being approximated in (13) have scales of $O(1)$ and $O(1/\sigma)$, respectively, by the following two estimates:

$$\mathbb{E}_{\tilde{x}|x} P(\tilde{x}) \nabla_{\tilde{x}} \log p_\sigma(\tilde{x}) = \mathbb{E}_{\tilde{x}|x} (P(x^*) + O(\tilde{x} - x^*)) \left(\frac{x^* - \tilde{x}}{\sigma^2} + O(1) \right) = O(1), \quad (14)$$

$$\mathbb{E}_{\tilde{x}|x} P^\perp(\tilde{x}) \nabla_{\tilde{x}} \log p_\sigma(\tilde{x}) = \mathbb{E}_{\tilde{x}|x} (P^\perp(x^*) + O(\tilde{x} - x^*)) \left(\frac{x^* - \tilde{x}}{\sigma^2} + O(1) \right) = O\left(\frac{1}{\sigma}\right). \quad (15)$$

This multiscale singularity of the loss formulation poses significant challenges during training. Since the training loss (5) is essentially a quadratic loss (4), it inherently prioritizes fitting larger-scale features of the score, which are aligned with the normal component in our settings. This is because quadratic loss minimizes the average of squared errors, making it disproportionately sensitive to larger errors that predominantly occur in higher-scale directions. In the context of this work, the normal component pulls samples back onto the manifold, whereas the tangential component, which is more critical, captures the data distribution on the manifold. As a result, the model fails to adequately capture finer details of the data distribution, ultimately reducing the accuracy of the generated distribution. In other words, the trained model primarily captures the manifold itself rather than the distribution on it, leading to a phenomenon known as *manifold overfitting* [18].

To address these limitations, specific methods are required during the model training phase to ensure training stability and accurately capture the intrinsic data distribution on the manifold. Based on

this perspective, we propose the following two solutions: First, the scale discrepancy between the tangential and normal components can be reduced by modifying the structure of the noise. Second, instead of explicitly considering the normal component of the score function, its role in projecting samples back onto the manifold during generation is delegated to a dedicated projection operator.

4 Methods

In this section, we propose two methods to address the singularity of the score function. The first method, referred to as Niso-DM, introduces additional noise along the normal direction to mitigate its dominance. The second method, called Tango-DM, focuses only on the training of the tangential component of the score function when the noise scale σ_t is small.

4.1 Niso-DM: Perturb data with non-isotropic noise

We propose a strategy to mitigate scale discrepancies by replacing the isotropic noise in the forward process of diffusion models with non-isotropic noise. The perturbed data is generated as $\tilde{x}_t = x + \sigma_t \epsilon_1 + \sigma_t^{\alpha_t} N(x) \epsilon_2$, where $x \sim p_0(x)$, $\epsilon_1 \sim \mathcal{N}(0, I_n)$, $\epsilon_2 \sim \mathcal{N}(0, I_{n-d})$, $\alpha_t \in (0, 1)$, and $N(x) \in \mathbb{R}^{n \times (n-d)}$ is defined in Section 2.2. The term $\sigma_t^{\alpha_t} N(x) \epsilon_2$ represents an additional noise along the normal direction. The conditional distribution of the perturbed data is given by $p_{\sigma_t}(\tilde{x}|x) = \mathcal{N}(x, \Sigma_{\sigma_t}(x))$, where $\Sigma_{\sigma_t}(x) = \sigma_t^2 I + \sigma_t^{2\alpha_t} N(x) N(x)^T$. The following Theorem establishes the relationship between $\nabla_{\tilde{x}} \log p_{\sigma_t}(\tilde{x})$ and $\nabla_{\tilde{x}} \log p_0(\tilde{x})$, as $\sigma_t \rightarrow 0$.

Theorem 4.1. *Let $p_{\sigma}(\tilde{x})$ denote the distribution under non-isotropic perturbation, defined as:*

$$p_{\sigma}(\tilde{x}) = \int_{\mathcal{M}} e^{-V_0(x)} (2\pi)^{-\frac{n}{2}} (\det \Sigma_{\sigma}(x))^{-\frac{1}{2}} e^{-\frac{1}{2}(\tilde{x}-x)^T \Sigma_{\sigma}(x)^{-1}(\tilde{x}-x)} d\sigma(x), \quad (16)$$

where $\Sigma_{\sigma}(x) = \sigma^2 I + \sigma^{2\alpha} N(x) N(x)^T$ and $\alpha \in (0, 1)$. By making the same assumptions as in Theorem 3.1, and $M_2 = \sup_{x \in \mathcal{M}} \max_{1 \leq k, l, j, j' \leq n} \left| \frac{\partial^2 P_{kl}}{\partial x_j \partial x_{j'}}(x) \right| < +\infty$, then we have the following results for $p_{\sigma}(\tilde{x})$:

1. For $\tilde{x} \notin \mathcal{M}$, assume that $x^* \in \mathcal{M}$ is the unique minimizer of $\min_{x \in \mathcal{M}} \|x - \tilde{x}\|$, and that $\|x^* - \tilde{x}\|_{\infty} < \min\{1, \frac{2}{n^2(4M_1 + M_2)}\}$. Under these conditions, as $\sigma \rightarrow 0$, we have

$$\nabla_{\tilde{x}} \log p_{\sigma}(\tilde{x}) = \frac{x^* - \tilde{x}}{\sigma^{2\alpha}} \cdot \frac{1}{1 + \sigma^{2-2\alpha}} + O(\sigma^{(1-2\alpha) \wedge 0}). \quad (17)$$

2. For $\tilde{x} \in \mathcal{M}$, as $\sigma \rightarrow 0$, we have

$$\nabla_{\tilde{x}} \log p_{\sigma}(\tilde{x}) = \nabla_{\tilde{x}}^{\mathcal{M}} \log p_0(\tilde{x}) + O(\sigma^{(2-2\alpha) \wedge 1}). \quad (18)$$

Eq. (17) shows that by introducing additional noise along the normal direction, the scale of the normal component is reduced from $O(1/\sigma^2)$ to $O(1/\sigma^{2\alpha})$ pointwise. Eq. (18) states that this approach does not affect the characterization of the distribution on the manifold (i.e., the tangential component). As the noise level parameter σ_t approaches zero, the score function of the perturbed distribution p_{σ_t} on the manifold converges to the Riemannian score function of p_0 . Therefore, by employing non-isotropic noise, we can still generate samples that adhere to the original distribution of the dataset.

Noting that $\nabla_{x_t} \log p_{\sigma_t}(x_t|x) = -\Sigma_{\sigma_t}(x)^{-1}(x_t - x)$, the denoising score matching loss (5) can be written into the following form:

$$\ell_{\text{Niso}}(t, \theta) = \mathbb{E}_{x, x_t} \|s_{\theta}(x_t, t) + \Sigma_{\sigma_t}(x)^{-1}(x_t - x)\|^2. \quad (19)$$

Under the settings in Section 2.2, $\Sigma_{\sigma_t}(x)^{-1}$ has a closed-form expression (See (50)). Besides, we set $\alpha_t = \log c_{\text{niso}} / \log \sigma_t$ (i.e., $c_{\text{niso}} = \sigma_t^{\alpha_t}$) in practice, where c_{niso} is a fixed constant.

4.2 Tango-DM: Learn only the tangential component of the score function

Recall that the projection matrix $P(x)$ can be continuously extended to the ambient space \mathbb{R}^n . Accordingly, we define $s_{\theta}^{\parallel}(x, t) := P(x) s_{\theta}(x, t)$ for $x \in \mathbb{R}^n$, which represents the tangential component of the parametrized vector field.

As discussed in (13), the loss function (4) can be decomposed into two parts, $\ell_{\text{quad}}^{\parallel}$ and $\ell_{\text{quad}}^{\perp}$, and the singularity issue primarily arises from the normal component $\ell_{\text{quad}}^{\perp}$. To address this, we propose training only the tangential component of the score function when the noise scale σ_t is sufficiently small, thereby avoiding the singularity associated with $\ell_{\text{quad}}^{\perp}$. To compute $\ell_{\text{quad}}^{\parallel}$, we introduce the following Tango loss,

$$\ell_{\text{tango}}(t, \theta) := \mathbb{E}_{x, x_t} \|s_{\theta}^{\parallel}(x_t, t) - P(x_t)\nabla_{x_t} \log p_{\sigma_t}(x_t|x)\|^2. \quad (20)$$

The optimal score network $s_{\theta^*}^{\parallel}(x, t)$ that minimizes (20) almost surely satisfies $s_{\theta^*}^{\parallel}(x, t) = P(x)\nabla_x \log p_{\sigma_t}(x)$. This result ensures the validity of the loss function in (20), with the proof provided in Appendix C.1.

When the noise scale is smaller than a pre-selected c_{tango} (i.e. $\sigma_t < c_{\text{tango}}$), the tangential component of the score function $s_{\theta}^{\parallel}(x, t)$ is trained via the Tango loss ℓ_{tango} . On the other hand, when $\sigma_t \geq c_{\text{tango}}$, the singularity issues are less severe, allowing us to use the original denoising score matching loss (5) to train the entire score function $s_{\theta}(x, t)$, which includes information along the normal direction. This enables the score function to push points toward the vicinity of the manifold. The overall loss calculation is summarized in Algorithm 1.

5 Generation

We propose two sampling methods to generate samples using the learned score function s_{θ} . The first method, named *Reverse SDE*, is based on the standard generation process in \mathbb{R}^n , with an additional projection step to ensure the samples lie on manifolds. The second method, named *Annealing SDE*, adopts a two-stage approach: the first stage simulates the reverse SDE, and the second stage performs annealed Langevin dynamics constrained to manifolds. The details of these methods are provided in the sections below and are summarized in Algorithms 2 and 3.

5.1 Reverse SDE

The Reverse SDE method follows the standard generation process, where samples are generated by simulating the reverse SDE (21), with t going from T to 0.

$$dX_t = -g(t)^2 s_{\theta}(X_t, t)dt + g(t)d\bar{W}_t \quad (21)$$

However, the ending samples lie in the vicinity of the manifold rather than exactly on it. To address this, we add a final projection step π to ensure that the generated points lie on the manifold.

In general, this method is not applicable to Tango-DM that involves Tango loss. Since the normal component of the score function is not learned when t is small, the score function $s_{\theta}(x, t)$ does not capture information in the normal direction. For Niso-DM method, the final distribution of the reverse SDE can be expressed as $x + c_{\text{niso}}N(x)\epsilon_2$, where $x \sim p_0$ and $c_{\text{niso}}N(x)\epsilon_2$ represents noise along the normal direction. By projection onto the manifold as the final step, the samples we obtain closely approximate the target distribution.

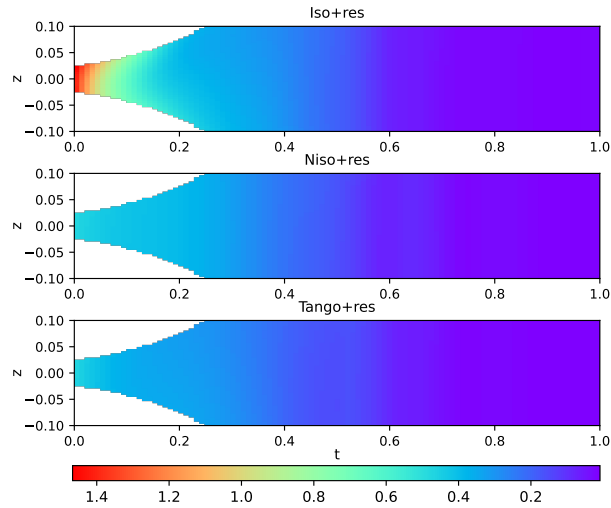


Figure 1: The average error of the tangential component of the learned score function in the $x - y$ plane, along the z -axis and t -axis. From top to bottom, the plots correspond to the vanilla algorithm (Iso-DM), our proposed Niso-DM and Tango-DM, all using the rescaling technique.

5.2 Annealing SDE on manifolds

The Annealing SDE method adopts a two-stage sampling procedure, divided by a predefined threshold $\tilde{\sigma}$. In the first stage ($\sigma_t \geq \tilde{\sigma}$), we simulate the reverse SDE (21), which provides a coarse approximation of the target distribution near the manifold. In the second stage ($\sigma_t < \tilde{\sigma}$), we refine the samples by simulating annealed Langevin dynamics constrained to the manifold. Specifically, for a fixed t , we perform n_0 steps of the following Langevin dynamics:

$$dX_s = P(X_s)s_\theta(X_s, t)ds + \sqrt{2}dW_s^{\mathcal{M}}. \quad (22)$$

After completing n_0 steps, we decrease t according to $t \leftarrow t - \Delta t$ and restart the simulation of SDE (22) using the final samples from the previous iteration as the initial states. This process is repeated until the desired level of refinement is achieved. i.e., $t = 0$. This stage can be viewed as the manifold version of the Corrector algorithms in [31].

To analysis the proposed sampling method, we assume that the neural network s_θ has learned the optimal solution, i.e. $P(x)s_\theta(x, t) = \nabla_x^{\mathcal{M}} \log p_{\sigma_t}(x)$ for $x \in \mathcal{M}$. Under this assumption, the invariant distribution of the SDE (22) is $p_{\sigma_t}(x)d\sigma_{\mathcal{M}}(x)$. According to (12) in Theorem 3.1 and (18) in Theorem 4.1, regardless of whether non-isotropic noise is used, $\nabla_x^{\mathcal{M}} \log p_{\sigma_t}(x)$ converges to $\nabla_x^{\mathcal{M}} \log p_0(x)$ as $t \rightarrow 0$. This demonstrates that by employing annealed Langevin dynamics constrained to the manifold, we can effectively sample from the target distribution $p_0(x)d\sigma_{\mathcal{M}}(x)$ on the manifold.

6 Experiments

Table 1: Results for the Hyperplane: MMD under different training methods. In this example, the Reverse SDE sampling method is applicable to Tango-DM due to the complete decoupling of tangential and normal components. For more detailed explanations, refer to the caption of Table 2.

	Reversal	Annealing
Iso	2.81e-4±5.66e-5	7.97e-4±6.89e-5
Niso	1.52e-4±2.60e-5	5.32e-4±3.03e-4
Tango	1.65e-4±3.91e-5	5.82e-4±1.17e-4
Iso+res	2.79e-4±9.41e-5	7.81e-4±2.69e-4
Niso+res	1.45e-4±2.68e-5	1.88e-4±4.49e-5
Tango+res	1.19e-4 ±1.96e-5	2.22e-4 ±3.03e-5

In this section, we evaluate our methods by addressing several representative problems on typical manifolds. Specifically, we consider four examples: (1) a toy model of the hyperplane in 3D space, (2) mesh manifolds in 3D space, (3) the special orthogonal group of order 10, and (4) the level set of collective variables in the alanine dipeptide system.

Furthermore, we also consider using neural networks to approximate the normalized score functions, i.e. $s_\theta(x, t) = \hat{s}_\theta(x, t)/w_t$, where $\hat{s}_\theta(x, t)$ denotes a neural network and w_t is the scaling factor of the optimal score function. This approach, which we refer to as the *rescaling technique*, is designed to improve numerical stability, as neural networks can more effectively approximate an $O(1)$ term compared to one that grows explosively. Notably, this technique is

equivalent to the ϵ -parameterization introduced in [26, 35].

We perform experiments with the vanilla diffusion models, as well as our proposed Niso-DM and Tango-DM, denoted as *Iso*, *Niso*, and *Tango*, respectively. The notation *+res* indicates the rescaling technique discussed above, which involves using neural networks to model the normalized score functions. After training, new samples are generated via two methods: Reverse SDE and Annealing SDE on manifolds. To evaluate the quality of the generated samples, we use several metrics to compare the generated distribution with the target distribution. We conduct our experiments using the same hyperparameters, except for those specific to each algorithm. *Overall, we recommend the Niso+res training algorithm combined with the Reverse SDE generation method, as it performs best in most cases.* Further details are provided in Appendix D. We also conduct ablation studies in Appendix E to analyze the bias-variance tradeoff associated with the choice of hyperparameters.

6.1 The hyperplane in 3D space

We first consider a toy model: the hyperplane embedded in a three-dimensional Euclidean space, specifically the set $\mathcal{M} = \{(x, y, z) \in \mathbb{R}^3 | z = 0\}$. The target distribution is a mixture of Gaussian

distributions with nine modes located on the plane. In this example, the score function has a closed-form solution that can be explicitly derived.

In Figure 1, we present the error of the tangential component of the score function. The results demonstrate that our proposed Niso-DM and Tango-DM significantly reduce the tangential component error, as t approaches 0. Table 1 in the Appendix reports the maximum mean discrepancy (MMD), where both Niso-DM and Tango-DM show significant performance improvements.

6.2 Mesh data

We consider the Standard Bunny [32] and Spot the Cow [5], which contain meshes derived from 3D scanning a ceramic figurine of a rabbit and a cow, respectively. To create the target densities, we follow the approach in [4, 14, 25], which utilizes the eigenpairs of the Laplace-Beltrami operator on meshes. The target distribution is chosen as an equal-proportion mixture of density functions corresponding to the 0-th, 500-th, and 1000-th eigenpairs.

Table 2 reports the Jensen–Shannon (JS) divergence of the histograms on mesh faces between the generated samples and the original datasets. With the Rescaling technique, both Niso-DM and Tango-DM demonstrate significant improvements; without it, the Tango-DM still achieves improvements under the Annealing algorithm.

Table 2: Results for Stanford Bunny and Spot the Cow: JS distance of the samples generated by the Reverse SDE and Annealing SDE algorithms under different training methods. The symbol "-" indicates that the Reverse SDE sampling method is not applicable to Tango-DM. The results are reported as the mean and standard deviation over five independent runs. The notation *+res* indicates the rescaling technique. The bold values represent the minimum value in each column (sampling algorithm).

	Stanford Bunny		Spot the Cow	
	Reversal	Annealing	Reversal	Annealing
Iso	3.58e-1±1.36e-3	4.95e-1±1.69e-1	3.41e-1±3.20e-3	3.65e-1±2.97e-3
Niso	3.58e-1±1.17e-3	4.12e-1±2.63e-3	3.38e-1±1.27e-3	3.68e-1±3.90e-3
Tango	-	4.08e-1±5.71e-4	-	3.51e-1±3.65e-3
Iso+res	3.52e-1±2.17e-3	3.94e-1±1.63e-3	3.30e-1±2.08e-3	3.48e-1±1.82e-3
Niso+res	3.48e-1 ±8.27e-4	3.86e-1±1.85e-3	3.28e-1 ±6.19e-4	3.40e-1±2.34e-3
Tango+res	-	3.84e-1 ±1.57e-3	-	3.39e-1 ±1.74e-3

6.3 High-dimensional special orthogonal group

We evaluate the performance of our method in a high-dimensional setting on the special orthogonal group $SO(10)$, a 45-dimensional submanifold embedded in \mathbb{R}^{100} . We construct a synthetic dataset drawn from a multimodal distribution on $SO(10)$, consisting of 5 modes.

Our results demonstrate the effectiveness of the proposed method. In Table 3, we compare the sliced 1-Wasserstein [1] distances between the generated and the target distributions. These findings highlight the precision and reliability of our approach in high co-dimensional manifold settings.

6.4 Alanine dipeptide

We apply our method to alanine dipeptide, a model system frequently examined in computational chemistry. The system’s configuration is characterized by two dihedral angles, ϕ and ψ (refer to Figure 2). The manifold consists of the configurations of the system’s 10 non-hydrogen atoms (in \mathbb{R}^{30}) with the angle ϕ fixed at -70° , which represents a level set of the reaction coordinate ϕ .

Table 4 exhibits the results of 1-Wasserstein distance between the test datasets and the generated samples, showing that our methods outperforms the vanilla models under both the Reverse SDE and the Annealing SDE sampling algorithms. However, in this case, training the normalized score functions (*+res*) does not lead to better results. One possible explanation is that it simultaneously

rescales both the tangential and normal components, resulting in the loss of critical tangential information.

Table 3: Results for SO(10): Sliced 1-Wasserstein distance under different training methods. For more detailed explanations, refer to the caption of Table 2.

	Reversal	Annealing
Iso	1.76e-2±1.15e-2	1.86e-2±9.65e-3
Niso	5.58e-3±1.84e-3	1.16e-2±2.51e-3
Tango	-	1.89e-2±2.05e-3
Iso+res	9.49e-3±1.91e-3	1.17e-2±7.29e-4
Niso+res	4.60e-3 ±8.24e-4	6.00e-3 ±7.53e-4
Tango+res	-	6.42e-3±1.97e-3

Table 4: Results for dipeptide: 1-Wasserstein distance under different training methods. For more detailed explanations, refer to the caption of Table 2.

	Reversal	Annealing
Iso	8.60e-2±5.29e-3	8.83e-2±9.32e-3
Niso	8.31e-2 ±5.29e-3	8.24e-2 ±5.96e-3
Tango	-	8.60e-2±5.71e-3
Iso+res	8.59e-2±6.90e-3	1.21e-1±6.66e-3
Niso+res	8.34e-2±5.56e-3	9.47e-2±5.61e-3
Tango+res	-	9.62e-2±9.14e-3

7 Related work

It is important to clarify that research on manifold-related diffusion models can be broadly categorized into two directions: (1) diffusion models for distributions under the manifold hypothesis, where the underlying manifold is unknown, and (2) diffusion models for distributions on a known manifold, which is the focus of this work. For the former, we discuss the singularity of score functions in related work; for the latter, we explore several studies based on known manifolds.

On the singularity of score functions Several studies on diffusion models under the manifold hypothesis [6, 21, 23] have highlighted the singularity of the score function, specifically identifying that as $t \rightarrow 0$, the score function diverges. Beyond empirical observations, recent studies have provided mathematical analysis of diffusion models based on the VPSDE. For instance, Chen et al. [2] presents a mathematical analysis under a linear assumption on the dataset, where each data point is assumed to lie on a hyperplane. In [23], it is shown that the score function norm satisfies $\mathbb{E}\|\nabla_x \log p_t(x)\| \gtrsim 1/\sqrt{t}$. Furthermore, Lu et al. [21] rigorously examines the asymptotic behavior of the score function as $t \rightarrow 0$ for the VPSDE, demonstrating that its singularity follows a $1/t$ scaling in a strong pointwise sense, which is similar to our results in (10). Further discussion can be found in [19].

To mitigate this singularity issue, a number of works (e.g. [31]) propose starting their analysis at $t = \epsilon > 0$, instead of $t = 0$. However, this approach is equivalent to selecting a larger σ_{\min} and does not fully resolve the fundamental singularity problem. The study [8] introduces a diffusion model on the product space of position and velocity, employing hybrid score matching to circumvent the singularity. Furthermore, in [30], the score function is parameterized by $s_\theta(x, t) = \hat{s}_\theta(x)/\sigma_t$, where $\hat{s}_\theta(x)$ is a neural network.

Diffusion models on manifolds Riemannian Score-based Generative Models [7] extend SDE-based diffusion models to manifold settings by estimating the transition kernels using either the eigenpairs of the Laplacian–Beltrami operator on manifolds [20] or the Varadhan approximation via the Riemannian logarithmic map. Riemannian Diffusion Models [13] employ a variational diffusion framework for Riemannian manifolds and, similar to our approach, consider submanifolds embedded in Euclidean space. Additionally, Trivialized Diffusion Models [37] introduce a technique called *trivialization* that adapts diffusion models from Euclidean spaces to Lie groups.

8 Conclusion

We address the multiscale singularity of the score function for manifold-constrained data, which limits the accuracy of Euclidean diffusion models in this work. By decomposing the score function into tangential and normal components, we identify the source of scale discrepancies and propose two methods: Niso-DM, which reduces discrepancies with non-isotropic noise, and Tango-DM,

which trains only the tangential component. Both methods achieve superior performance on complex manifolds, improving the accuracy and robustness of diffusion-based generative models.

References

- [1] Nicolas Bonneel, Julien Rabin, Gabriel Peyré, and Hanspeter Pfister. Sliced and radon wasserstein barycenters of measures. *Journal of Mathematical Imaging and Vision*, 51:22–45, 2015.
- [2] Minshuo Chen, Kaixuan Huang, Tuo Zhao, and Mengdi Wang. Score approximation, estimation and distribution recovery of diffusion models on low-dimensional data. In *International Conference on Machine Learning*, pages 4672–4712. PMLR, 2023.
- [3] Nanxin Chen, Yu Zhang, Heiga Zen, Ron J Weiss, Mohammad Norouzi, and William Chan. Wavegrad: Estimating gradients for waveform generation. In *International Conference on Learning Representations*, 2021.
- [4] Ricky T. Q. Chen and Yaron Lipman. Flow matching on general geometries. In *International Conference on Learning Representations*, 2024.
- [5] Keenan Crane, Ulrich Pinkall, and Peter Schröder. Robust fairing via conformal curvature flow. *ACM Transactions on Graphics (TOG)*, 32(4):1–10, 2013.
- [6] Valentin De Bortoli. Convergence of denoising diffusion models under the manifold hypothesis. *arXiv preprint arXiv:2208.05314*, 2022.
- [7] Valentin De Bortoli, Emile Mathieu, Michael Hutchinson, James Thornton, Yee Whye Teh, and Arnaud Doucet. Riemannian score-based generative modelling. In *Advances in Neural Information Processing Systems*, volume 35, pages 2406–2422, 2022.
- [8] Tim Dockhorn, Arash Vahdat, and Karsten Kreis. Score-based generative modeling with critically-damped langevin diffusion. *arXiv preprint arXiv:2112.07068*, 2021.
- [9] Jonathan Ho, Ajay Jain, and Pieter Abbeel. Denoising diffusion probabilistic models. In *Advances in Neural Information Processing Systems*, volume 33, pages 6840–6851, 2020.
- [10] Jonathan Ho, Chitwan Saharia, William Chan, David J Fleet, Mohammad Norouzi, and Tim Salimans. Cascaded diffusion models for high fidelity image generation. *Journal of Machine Learning Research*, 23(47):1–33, 2022.
- [11] Emiel Hoogeboom, Victor Garcia Satorras, Clément Vignac, and Max Welling. Equivariant diffusion for molecule generation in 3d. In *International conference on machine learning*, pages 8867–8887. PMLR, 2022.
- [12] Hugues Hoppe, Tony DeRose, Tom Duchamp, John McDonald, and Werner Stuetzle. Surface reconstruction from unorganized points. In *Proceedings of the 19th annual conference on computer graphics and interactive techniques*, pages 71–78, 1992.
- [13] Chin-Wei Huang, Milad Aghajohari, Joey Bose, Prakash Panangaden, and Aaron Courville. Riemannian diffusion models. In *Advances in Neural Information Processing Systems*, volume 35, pages 2750–2761, 2022.
- [14] Jaehyeong Jo and Sung Ju Hwang. Generative modeling on manifolds through mixture of Riemannian diffusion processes. In *International Conference on Machine Learning*, volume 235, pages 22348–22370. PMLR, 2024.
- [15] Anna Klimovskaia, David Lopez-Paz, Léon Bottou, and Maximilian Nickel. Poincaré maps for analyzing complex hierarchies in single-cell data. *Nature communications*, 11(1):2966, 2020.
- [16] Haoying Li, Yifan Yang, Meng Chang, Shiqi Chen, Huajun Feng, Zhihai Xu, Qi Li, and Yueting Chen. Srdiff: Single image super-resolution with diffusion probabilistic models. *Neurocomputing*, 479:47–59, 2022.
- [17] Zichen Liu, Wei Zhang, Christof Schütte, and Tiejun Li. Riemannian denoising diffusion probabilistic models, 2025. URL <https://arxiv.org/abs/2505.04338>.
- [18] Gabriel Loaiza-Ganem, Brendan Leigh Ross, Jesse C Cresswell, and Anthony L Caterini. Diagnosing and fixing manifold overfitting in deep generative models. *arXiv preprint arXiv:2204.07172*, 2022.

- [19] Gabriel Loaiza-Ganem, Brendan Leigh Ross, Rasa Hosseinzadeh, Anthony L Caterini, and Jesse C Cresswell. Deep generative models through the lens of the manifold hypothesis: A survey and new connections. *arXiv preprint arXiv:2404.02954*, 2024.
- [20] Aaron Lou, Minkai Xu, Adam Farris, and Stefano Ermon. Scaling Riemannian diffusion models. In *Advances in Neural Information Processing Systems*, volume 36, pages 80291–80305, 2023.
- [21] Yubin Lu, Zhongjian Wang, and Guillaume Bal. Mathematical analysis of singularities in the diffusion model under the submanifold assumption. *arXiv preprint arXiv:2301.07882*, 2023.
- [22] Emile Mathieu and Maximilian Nickel. Riemannian continuous normalizing flows. In *Advances in Neural Information Processing Systems*, volume 33, pages 2503–2515, 2020.
- [23] Jakiw Pidstrigach. Score-based generative models detect manifolds. *Advances in Neural Information Processing Systems*, 35:35852–35865, 2022.
- [24] Boris T Polyak and Anatoli B Juditsky. Acceleration of stochastic approximation by averaging. *SIAM Journal on Control and Optimization*, 30(4):838–855, 1992.
- [25] Noam Rozen, Aditya Grover, Maximilian Nickel, and Yaron Lipman. Moser flow: Divergence-based generative modeling on manifolds. *Advances in Neural Information Processing Systems*, 34:17669–17680, 2021.
- [26] Tim Salimans and Jonathan Ho. Progressive distillation for fast sampling of diffusion models. In *International Conference on Learning Representations*, 2022.
- [27] Anthony Simeonov, Yilun Du, Andrea Tagliasacchi, Joshua B Tenenbaum, Alberto Rodriguez, Pulkit Agrawal, and Vincent Sitzmann. Neural descriptor fields: Se (3)-equivariant object representations for manipulation. In *2022 International Conference on Robotics and Automation (ICRA)*, pages 6394–6400. IEEE, 2022.
- [28] Jascha Sohl-Dickstein, Eric Weiss, Niru Maheswaranathan, and Surya Ganguli. Deep unsupervised learning using nonequilibrium thermodynamics. In *International Conference on Machine Learning*, volume 37, pages 2256–2265. PMLR, 2015.
- [29] Yang Song and Stefano Ermon. Generative modeling by estimating gradients of the data distribution. In *Advances in Neural Information Processing Systems*, volume 32, pages 11895–11907, 2019.
- [30] Yang Song and Stefano Ermon. Improved techniques for training score-based generative models. *Advances in neural information processing systems*, 33:12438–12448, 2020.
- [31] Yang Song, Jascha Sohl-Dickstein, Diederik P Kingma, Abhishek Kumar, Stefano Ermon, and Ben Poole. Score-based generative modeling through stochastic differential equations. In *International Conference on Learning Representations*, 2021.
- [32] Greg Turk and Marc Levoy. Zippered polygon meshes from range images. In *Proceedings of the 21st Annual Conference on Computer Graphics and Interactive Techniques*, pages 311–318, 1994.
- [33] Pascal Vincent. A connection between score matching and denoising autoencoders. *Neural computation*, 23(7):1661–1674, 2011.
- [34] Joseph L Watson, David Juergens, Nathaniel R Bennett, Brian L Trippe, Jason Yim, Helen E Eisenach, Woody Ahern, Andrew J Borst, Robert J Ragotte, Lukas F Milles, et al. Broadly applicable and accurate protein design by integrating structure prediction networks and diffusion generative models. *BioRxiv*, pages 2022–12, 2022.
- [35] Ling Yang, Zhilong Zhang, Yang Song, Shenda Hong, Runsheng Xu, Yue Zhao, Wentao Zhang, Bin Cui, and Ming-Hsuan Yang. Diffusion models: A comprehensive survey of methods and applications. *ACM Computing Surveys*, 56(4):1–39, 2023.
- [36] Linqi Zhou, Yilun Du, and Jiajun Wu. 3d shape generation and completion through point-voxel diffusion. In *Proceedings of the IEEE/CVF international conference on computer vision*, pages 5826–5835, 2021.
- [37] Yuchen Zhu, Tianrong Chen, Ling kai Kong, Evangelos Theodorou, and Molei Tao. Trivialized momentum facilitates diffusion generative modeling on lie groups. In *The Thirteenth International Conference on Learning Representations*, 2025.

A Proof for Theorem 3.1

Preparation. For simplicity of notation, we use $|\cdot|$ to denote the Euclidean norm in the following two sections. Let us recall the expression

$$p_\sigma(\tilde{x}) = \int_{\mathcal{M}} p_0(x) p_\sigma(\tilde{x}|x) d\sigma_{\mathcal{M}}(x), \quad \sigma > 0. \quad (23)$$

Let $x^* \in \mathcal{M}$ be the unique minimizer of the minimization

$$\min_{x \in \mathcal{M}} |x - \tilde{x}|. \quad (24)$$

In the following, we study the limit of integrals over \mathcal{M} as $\sigma \rightarrow 0$ by a change of variables using the exponential map on \mathcal{M} at x^* . To this end, let us first derive some asymptotic expressions related to the exponential map.

Denote by $T_{x^*}\mathcal{M} = \{v | \nabla \xi(x^*)^T v = 0, v \in \mathbb{R}^n\}$ the tangent space of \mathcal{M} at x^* . Given $v \in T_{x^*}\mathcal{M}$, let $\gamma_v(t) \in \mathbb{R}^n$ be the geodesic curve on \mathcal{M} starting from $\gamma_v(0) = x^*$ at $t = 0$ such that $\dot{\gamma}_v(0) = d\gamma_v(t)/dt(0) = v$. We have Taylor's expansion

$$\gamma_v(t) = x^* + vt + \frac{1}{2} \ddot{\gamma}_v(0) t^2 + O(t^3), \quad \text{as } t \rightarrow 0. \quad (25)$$

Since $x^* = \gamma_v(0)$ is the minimizer of (24), we know that $|\gamma_v(t) - \tilde{x}|^2$ (as a function of t) attains its minimum at $t = 0$. Therefore, taking derivative and setting $t = 0$, we obtain

$$v \cdot (x^* - \tilde{x}) = 0, \quad \forall v \in T_{x^*}\mathcal{M}. \quad (26)$$

An expression for the second-order derivative $\ddot{\gamma}_v(0)$ in (25) is not available in general. However, by differentiating the identity $(I - P(\gamma_v(t)))\dot{\gamma}_v(t) = 0$ with respect to t , where and setting $t = 0$, we obtain the equation (i.e. the expression for the orthogonal component of $\ddot{\gamma}_v(0)$)

$$(I - P(x^*))\ddot{\gamma}_v(0) = \sum_{1 \leq j, j' \leq n} \frac{\partial P_{\cdot j}}{\partial x_{j'}}(x^*) v_j v_{j'}, \quad (27)$$

where $\frac{\partial P_{\cdot i}}{\partial x_{j'}}(x^*)$ denotes the vector in \mathbb{R}^n whose i -th component is $\frac{\partial P_{ij}}{\partial x_{j'}}(x^*)$, for $1 \leq i \leq n$.

The exponential map $\exp_{x^*} : T_{x^*}\mathcal{M} \rightarrow \mathcal{M}$ is well-defined in the neighbourhood \mathcal{O} of $v = 0 \in T_{x^*}\mathcal{M}$, and it is related to the geodesic curves by $\exp_{x^*}(v) = \gamma_{\hat{v}}(|v|)$, where $\hat{v} = v/|v|$. Therefore, from (25) we have

$$\exp_{x^*}(v) = x^* + v + \frac{|v|^2}{2} \ddot{\gamma}_{\hat{v}}(0) + O(|v|^3), \quad \text{as } |v| \rightarrow 0. \quad (28)$$

Next, let us derive an expression for $|\exp_{x^*}(v) - \tilde{x}|^2$ when $|v|$ is small. Using (26) and (28), we can obtain

$$|\exp_{x^*}(v) - \tilde{x}|^2 = |x^* - \tilde{x}|^2 + |v|^2 \left(1 + \ddot{\gamma}_{\hat{v}}(0) \cdot (x^* - \tilde{x})\right) + O(|v|^3), \quad \text{as } |v| \rightarrow 0. \quad (29)$$

Noticing that $x^* - \tilde{x}$ is orthogonal to the tangent space $T_{x^*}\mathcal{M}$ (see (26)), using (27) we can compute the second term on the right hand side of (29)

$$|v|^2 \ddot{\gamma}_{\hat{v}}(0) \cdot (x^* - \tilde{x}) = |v|^2 \left((I - P(x^*)) \ddot{\gamma}_{\hat{v}}(0) \right) \cdot (x^* - \tilde{x}) = \sum_{1 \leq i, j, j' \leq n} \frac{\partial P_{ij}}{\partial x_{j'}}(x^*) v_j v_{j'} (x_i^* - \tilde{x}_i). \quad (30)$$

Substituting the above expression into (29) we get

$$|\exp_{x^*}(v) - \tilde{x}|^2 = |x^* - \tilde{x}|^2 + v^T S v + O(|v|^3), \quad \text{as } |v| \rightarrow 0, \quad (31)$$

where $S \in \mathbb{R}^{n \times n}$ is a matrix whose entries are

$$S_{jj'} = \delta_{jj'} + \frac{1}{2} \sum_{i=1}^n \left(\frac{\partial P_{ij'}}{\partial x_j} + \frac{\partial P_{ij}}{\partial x_{j'}} \right) (x^*) (x_i^* - \tilde{x}_i), \quad \text{for } 1 \leq j, j' \leq n. \quad (32)$$

From the Gershgorin circle theorem, all eigenvalues of S are greater than $1 - \frac{1}{2} \max_j \sum_{i, j'} \left| \left(\frac{\partial P_{ij'}}{\partial x_j} + \frac{\partial P_{ij}}{\partial x_{j'}} \right) (x^*) (x_i^* - \tilde{x}_i) \right|$. Furthermore, this lower bound is positive, as $\|x^* - \tilde{x}\|_\infty < \frac{1}{n^2 M_1}$. Therefore, the matrix S is positive definite. With the above expansions, we prove the two claims.

Proof of the first claim. We consider the general case where $\tilde{x} \in \mathbb{R}^n$ may not belong to \mathcal{M} . Since p_σ is the probability density of Gaussian distribution, we can derive

$$\begin{aligned}\nabla_{\tilde{x}} \log p_\sigma(\tilde{x}) &= \frac{1}{p_\sigma(\tilde{x})} \int_{\mathcal{M}} p_0(x) \frac{x - \tilde{x}}{\sigma^2} p_\sigma(\tilde{x}|x) d\sigma_{\mathcal{M}}(x) \\ &= \frac{x^* - \tilde{x}}{\sigma^2} + \frac{1}{p_\sigma(\tilde{x})} \int_{\mathcal{M}} p_0(x) \frac{x - x^*}{\sigma^2} p_\sigma(\tilde{x}|x) d\sigma_{\mathcal{M}}(x).\end{aligned}\quad (33)$$

On the one hand, since x^* is the unique minimizer of (24), there exists $\delta > 0$, such that $|x - \tilde{x}| \geq |x^* - \tilde{x}| + \delta$ for all $x \in \mathcal{M} \setminus \mathcal{O}'$, where $\mathcal{O}' := \exp_{x^*}(\mathcal{O})$. Therefore, we have

$$\begin{aligned}& \left| \int_{\mathcal{M} \setminus \mathcal{O}'} p_0(x) \frac{x - x^*}{\sigma^2} p_\sigma(\tilde{x}|x) d\sigma_{\mathcal{M}}(x) \right| \\ & \leq (2\pi\sigma^2)^{-\frac{n}{2}} \left[\int_{\mathcal{M} \setminus \mathcal{O}'} p_0(x) |x - x^*| d\sigma_{\mathcal{M}}(x) \right] (\sigma^{-2} e^{-\frac{\delta}{2\sigma^2}}) e^{-\frac{|x^* - \tilde{x}|^2}{2\sigma^2}} \\ & = o(e^{-\frac{\delta}{4\sigma^2}}) e^{-\frac{|x^* - \tilde{x}|^2}{2\sigma^2}}.\end{aligned}\quad (34)$$

On the other hand, using the fact that \exp_{x^*} is a diffeomorphism on \mathcal{O} with $|\det D \exp_{x^*}(v)| \equiv 1$, applying the change of variables $x = \exp_{x^*}(v)$, we get

$$\begin{aligned}& \int_{\mathcal{O}'} p_0(x) \frac{x - x^*}{\sigma^2} p_\sigma(\tilde{x}|x) d\sigma_{\mathcal{M}}(x) \\ & = (2\pi\sigma^2)^{-\frac{n}{2}} \int_{\mathcal{O}} p_0(\exp_{x^*}(v)) \frac{\exp_{x^*}(v) - x^*}{\sigma^2} e^{-\frac{|\exp_{x^*}(v) - \tilde{x}|^2}{2\sigma^2}} dv.\end{aligned}\quad (35)$$

Using the expansion (28), we can write

$$p_0(\exp_{x^*}(v))(\exp_{x^*}(v) - x^*) = p_0(x^*)v + \frac{1}{2}|v|^2 p_0(x^*)\ddot{\gamma}_{\tilde{v}}(0) + (\nabla^{\mathcal{M}} p_0(x^*) \cdot v)v + O(|v|^3). \quad (36)$$

Hence, using the expansions (31) and (36), we can derive the integral in (35) as

$$\begin{aligned}& \int_{\mathcal{O}'} p_0(x) \frac{x - x^*}{\sigma^2} p_\sigma(\tilde{x}|x) d\sigma_{\mathcal{M}}(x) \\ & = \int_{\mathcal{O}} \frac{1}{\sigma^2} \left(p_0(x^*)v + (\nabla^{\mathcal{M}} p_0(x^*) \cdot v)v + \frac{1}{2}|v|^2 p_0(x^*)\ddot{\gamma}_{\tilde{v}}(0) + O(|v|^3) \right) e^{-\frac{v^T S v + O(|v|^3)}{2\sigma^2}} dv \\ & \quad \cdot (2\pi\sigma^2)^{-\frac{n}{2}} e^{-\frac{|x^* - \tilde{x}|^2}{2\sigma^2}} \\ & = \int_{\mathcal{O}_\sigma} \left[p_0(x^*) \frac{v'}{\sigma} + (\nabla^{\mathcal{M}} p_0(x^*) \cdot v')v' + \frac{1}{2}|v'|^2 p_0(x^*)\ddot{\gamma}_{\tilde{v}'}(0) + O(\sigma) \right] e^{-\frac{v'^T S v' + O(\sigma)}{2}} dv' \\ & \quad \cdot (2\pi)^{-\frac{n}{2}} \sigma^{d-n} e^{-\frac{|x^* - \tilde{x}|^2}{2\sigma^2}} \\ & = O(1) \sigma^{d-n} e^{-\frac{|x^* - \tilde{x}|^2}{2\sigma^2}},\end{aligned}\quad (37)$$

where the second equality follows from a change of variables by $v = \sigma v'$ and $\mathcal{O}_\sigma := \{\sigma^{-1}v | v \in \mathcal{O}\}$, and the last equality follows from the fact that the integral $\int_{\mathcal{O}_\sigma} \frac{v'}{\sigma} e^{-\frac{v'^T S v' + O(\sigma)}{2}} dv'$ is $O(1)$. Combining (34) and (37), we arrive at

$$\int_{\mathcal{M}} p_0(x) \frac{x - x^*}{\sigma^2} p_\sigma(\tilde{x}|x) d\sigma_{\mathcal{M}}(x) = O(1) \sigma^{d-n} e^{-\frac{|x^* - \tilde{x}|^2}{2\sigma^2}}. \quad (38)$$

Using a similar derivation, for p_σ we can obtain the expansion

$$p_\sigma(\tilde{x}) = \int_{\mathcal{M}} p_0(x) p_\sigma(\tilde{x}|x) d\sigma_{\mathcal{M}}(x) = (2\pi\sigma^2)^{\frac{d-n}{2}} e^{-\frac{|x^* - \tilde{x}|^2}{2\sigma^2}} (p_0(x^*) + O(\sigma)). \quad (39)$$

The first claim is obtained by combining (33), (38), and (39).

Proof of the second claim. Now we consider the case where $\tilde{x} \in \mathcal{M}$. First of all, notice that in this case $S = I$ and (39) simplifies to

$$p_\sigma(\tilde{x}) = (2\pi\sigma^2)^{\frac{d-n}{2}} (p_0(\tilde{x}) + O(\sigma)). \quad (40)$$

We can derive

$$\begin{aligned} \nabla_{\tilde{x}} p_\sigma(\tilde{x}) &= - \int_{\mathcal{M}} p_0(x) \nabla_x p_\sigma(\tilde{x}|x) d\sigma_{\mathcal{M}}(x) \\ &= - \int_{\mathcal{M}} p_0(x) P(x) \nabla_x p_\sigma(\tilde{x}|x) d\sigma_{\mathcal{M}}(x) - \int_{\mathcal{M}} p_0(x) (I - P(x)) \nabla_x p_\sigma(\tilde{x}|x) d\sigma_{\mathcal{M}}(x) \\ &= - \int_{\mathcal{M}} p_0(x) \nabla_x^{\mathcal{M}} p_\sigma(\tilde{x}|x) d\sigma_{\mathcal{M}}(x) - \int_{\mathcal{M}} p_0(x) (I - P(x)) \nabla_x p_\sigma(\tilde{x}|x) d\sigma_{\mathcal{M}}(x) \\ &= \int_{\mathcal{M}} \nabla_x^{\mathcal{M}} p_0(x) p_\sigma(\tilde{x}|x) d\sigma_{\mathcal{M}}(x) + \int_{\mathcal{M}} p_0(x) (I - P(x)) \frac{x - \tilde{x}}{\sigma^2} p_\sigma(\tilde{x}|x) d\sigma_{\mathcal{M}}(x), \end{aligned} \quad (41)$$

where $\nabla_x^{\mathcal{M}}$ denotes the gradient operator on \mathcal{M} at x and we used the fact that $\nabla_x^{\mathcal{M}} = P(x) \nabla_x$ to obtain the third equality, and the last equality follows by using the integration by parts formula on \mathcal{M} .

For the first term in the last line of (41), similar to (39), we can obtain

$$\int_{\mathcal{M}} \nabla_x^{\mathcal{M}} p_0(x) p_\sigma(\tilde{x}|x) d\sigma_{\mathcal{M}}(x) = (2\pi\sigma^2)^{\frac{d-n}{2}} (\nabla_x^{\mathcal{M}} p_0(\tilde{x}) + O(\sigma)). \quad (42)$$

For the second term in the last line of (41), in analogy to (37), we derive

$$\begin{aligned} &\int_{\mathcal{O}'} p_0(x) (I - P(x)) \frac{x - \tilde{x}}{\sigma^2} p_\sigma(\tilde{x}|x) d\sigma_{\mathcal{M}}(x) \\ &= (2\pi\sigma^2)^{-\frac{n}{2}} \int_{\mathcal{O}} p_0(\exp_{\tilde{x}}(v)) (I - P(\exp_{\tilde{x}}(v))) \frac{\exp_{\tilde{x}}(v) - \tilde{x}}{\sigma^2} e^{-\frac{|\exp_{\tilde{x}}(v) - \tilde{x}|^2}{\sigma^2}} dv. \end{aligned} \quad (43)$$

The expansion (31) reduces to

$$|\exp_{\tilde{x}}(v) - \tilde{x}|^2 = |v|^2 + O(|v|^3), \quad (44)$$

and applying (28) we have

$$\begin{aligned} &(I - P(\exp_{\tilde{x}}(v))) (\exp_{\tilde{x}}(v) - \tilde{x}) \\ &= \frac{1}{2} (I - P(\tilde{x})) \ddot{\gamma}_{\tilde{x}}(0) |v|^2 - \sum_{1 \leq j, j' \leq d} \frac{\partial P_{\cdot j}}{\partial x_{j'}}(\tilde{x}) v_j v_{j'} + O(|v|^3) \\ &= -\frac{1}{2} \sum_{1 \leq j, j' \leq n} \frac{\partial P_{\cdot j}}{\partial x_{j'}}(\tilde{x}) v_j v_{j'} + O(|v|^3), \end{aligned} \quad (45)$$

where we have used (26) and (27) to derive the first and the second equality, respectively. We denote $U \in \mathbb{R}^{n \times d}$ whose columns form an orthonormal basis of $T_x \mathcal{M}$. It is straightforward to verify that

$U^T U = I \in \mathbb{R}^{d \times d}$ and $P(\tilde{x}) = U U^T$. We can compute (43) as

$$\begin{aligned}
& \int_{\mathcal{O}'} p_0(x) (I - P(x)) \frac{x - \tilde{x}}{\sigma^2} p_\sigma(\tilde{x}|x) d\sigma_{\mathcal{M}}(x) \\
&= (2\pi\sigma^2)^{-\frac{n}{2}} \int_{\mathcal{O}} (p_0(\tilde{x}) + O(|v|)) \frac{1}{\sigma^2} \left(-\frac{1}{2} \sum_{1 \leq j, j' \leq n} \frac{\partial P_{\cdot j}}{\partial x_{j'}}(\tilde{x}) v_j v_{j'} + O(|v|^3) \right) e^{-\frac{|v|^2 + O(|v|^3)}{2\sigma^2}} dv \\
&= (2\pi\sigma^2)^{\frac{d-n}{2}} \int_{\mathcal{O}_\sigma} (p_0(\tilde{x}) + O(\sigma)) \left[-\frac{1}{2} \sum_{1 \leq j, j' \leq n} \frac{\partial P_{\cdot j}}{\partial x_{j'}}(\tilde{x}) v'_j v'_{j'} + O(\sigma) \right] e^{-\frac{|v'|^2 + O(\sigma)}{2}} dv' \\
&= (2\pi\sigma^2)^{\frac{d-n}{2}} \int_{\mathcal{W}_\sigma} \left[-p_0(\tilde{x}) \frac{1}{2} \sum_{1 \leq j, j' \leq n} \frac{\partial P_{\cdot j}}{\partial x_{j'}}(\tilde{x}) \left(\sum_{l=1}^d U_{jl} w_l \right) \left(\sum_{l'=1}^d U_{j'l'} w_{l'} \right) + O(\sigma) \right] e^{-\frac{|Uw|^2 + O(\sigma)}{2}} dw \\
&= (2\pi\sigma^2)^{\frac{d-n}{2}} \int_{\mathcal{W}_\sigma} \left[-p_0(\tilde{x}) \frac{1}{2} \sum_{1 \leq j, j' \leq n} \frac{\partial P_{\cdot j}}{\partial x_{j'}}(\tilde{x}) (U U^T)_{jj'} + O(\sigma) \right] e^{-\frac{|w|^2 + O(\sigma)}{2}} dw \\
&= (2\pi\sigma^2)^{\frac{d-n}{2}} \left[-p_0(\tilde{x}) \frac{1}{2} \sum_{j, j'=1}^n \frac{\partial P_{\cdot j}}{\partial x_{j'}}(\tilde{x}) P_{jj'}(\tilde{x}) + O(\sigma) \right], \tag{46}
\end{aligned}$$

where the third equality follows from a further change of variables with $v' = Uw$ and $\mathcal{W}_\sigma = \{\sigma^{-1}U^T v | v \in \mathcal{O}\}$, the fourth equality follows from $|Uw|^2 = |w|^2$ and the fact that the integral converges to an integral with respect to a standard Gaussian density. Combining (41), (42), and (46), and using the fact that the corresponding integral on $\mathcal{M} \setminus \mathcal{O}'$ is $o(e^{-\frac{\delta}{4\sigma^2}})$, we derive (11) from

$$\nabla_{\tilde{x}} \log p_\sigma(\tilde{x}) = \frac{\nabla_{\tilde{x}} p_\sigma(\tilde{x})}{p_\sigma(\tilde{x})} = \nabla_{\tilde{x}}^{\mathcal{M}} \log p_0(\tilde{x}) - \frac{1}{2} \sum_{j, j'=1}^n \frac{\partial P_{\cdot j}}{\partial x_{j'}}(\tilde{x}) P_{jj'}(\tilde{x}) + O(\sigma). \tag{47}$$

Finally, define $T(\tilde{x}) = \sum_{j, j'=1}^n \frac{\partial P_{\cdot j}}{\partial x_{j'}}(\tilde{x}) P_{jj'}(\tilde{x})$, and we have

$$\begin{aligned}
T(\tilde{x}) &= \sum_{j, j'=1}^n \frac{\partial P_{\cdot j}}{\partial x_{j'}} P_{jj'} = \sum_{i, j, j'=1}^n \frac{\partial (P_{\cdot i} P_{ij})}{\partial x_{j'}} P_{jj'} \\
&= \sum_{i, j, j'=1}^n \frac{\partial P_{\cdot i}}{\partial x_{j'}} P_{ij} P_{jj'} + P_{\cdot i} \frac{\partial P_{ij}}{\partial x_{j'}} P_{jj'} = T(\tilde{x}) + P(\tilde{x}) T(\tilde{x}).
\end{aligned} \tag{48}$$

This implies that $P(\tilde{x}) T(\tilde{x}) = 0$. Therefore, multiplying $P(\tilde{x})$ on both sides of (47) confirms (12). Therefore, the second claim is obtained.

B Proof for Theorem 4.1

Preparation. We first study the properties of $\Sigma_\sigma(x)$. Recall that

$$\Sigma_\sigma(x) = \sigma^2 I + \sigma^{2\alpha} \nabla \xi(x) (\nabla \xi(x)^T \nabla \xi(x))^{-1} \nabla \xi(x)^T = \sigma^2 I + \sigma^{2\alpha} N(x) N(x)^T. \tag{49}$$

By the Sherman–Morrison–Woodbury Formula,

$$\begin{aligned}
\Sigma_\sigma(x)^{-1} &= \frac{1}{\sigma^2} \left(I - \frac{1}{1 + \sigma^{2-2\alpha}} N(x) N(x)^T \right) \\
&= \frac{1}{\sigma^2} P(x) + \frac{1}{\sigma^{2\alpha}} \frac{1}{1 + \sigma^{2-2\alpha}} (I - P(x)).
\end{aligned} \tag{50}$$

Besides,

$$\det \Sigma_\sigma(x) = \sigma^{2d} (\sigma^{2\alpha})^{n-d} (1 + \sigma^{2-2\alpha})^{n-d}. \tag{51}$$

Proof of the first claim. We first estimate the order of the following quadratic form:

$$\begin{aligned} & (x - \tilde{x})^T \Sigma_\sigma(x)^{-1} (x - \tilde{x}) \\ &= \frac{1}{\sigma^2} (x - \tilde{x})^T P(x) (x - \tilde{x}) + \frac{1}{\sigma^{2\alpha}} \frac{1}{1 + \sigma^{2-2\alpha}} (x - \tilde{x})^T (I - P(x)) (x - \tilde{x})^T. \end{aligned} \quad (52)$$

We apply the same change of variables $x = \exp_{x^*}(v)$ as the proof in Section A and $x = x^* - \tilde{x} + v + O(|v|^2)$. We obtain

$$\begin{aligned} & (x - \tilde{x})^T (I - P(x)) (x - \tilde{x})^T \\ &= \left(x^* - \tilde{x} + v + O(|v|^2) \right)^T \left(I - P(x^*) - \sum_k \frac{\partial P(x^*)}{\partial x_k} v_k + O(|v|^2) \right) \left(x^* - \tilde{x} + v + O(|v|^2) \right) \\ &= |x^* - \tilde{x}|^2 + O(|v|^2), \end{aligned} \quad (53)$$

$$\begin{aligned} & (x - \tilde{x})^T P(x) (x - \tilde{x}) \\ &= \left(x^* - \tilde{x} + v + O(|v|^2) \right)^T \left(P(x^*) + \sum_k \frac{\partial P(x^*)}{\partial x_k} v_k + \frac{1}{2} \sum_{k,l} \frac{\partial^2 P(x^*)}{\partial x_k \partial x_l} v_k v_l + O(|v|^3) \right) \\ & \quad \cdot \left(x^* - \tilde{x} + v + O(|v|^2) \right) \\ &= |v|^2 + 2 \sum_{k,j,j'} \frac{\partial P_{jj'}}{\partial x_k} (x^*) v_k v_{j'} (x_j^* - \tilde{x}_j) + \frac{1}{2} \sum_{k,l,j,j'} \frac{\partial^2 P(x^*)}{\partial x_k \partial x_l} v_k v_l (x_j^* - \tilde{x}_j) (x_{j'}^* - \tilde{x}_{j'}) + O(|v|^3) \\ &:= v^T \tilde{S} v + O(|v|^3). \end{aligned} \quad (54)$$

The disappearance of the first-order terms in (53) and (54) is attributed to

$$\begin{aligned} & (x^* - \tilde{x})^T \left(\sum_k \frac{\partial P(x^*)}{\partial x_k} v_k \right) (x^* - \tilde{x}) \\ &= (x^* - \tilde{x})^T \left(\sum_k \frac{\partial (P)^2(x^*)}{\partial x_k} v_k \right) (x^* - \tilde{x}) \\ &= (x^* - \tilde{x})^T P(x^*)^T \left(\sum_k \frac{\partial P(x^*)}{\partial x_k} v_k \right) (x^* - \tilde{x}) + (x^* - \tilde{x})^T \left(\sum_k \frac{\partial P(x^*)}{\partial x_k} v_k \right) P(x^*) (x^* - \tilde{x}) \\ &= 0, \end{aligned} \quad (55)$$

and $\tilde{S} \in \mathbb{R}^{n \times n}$ is a matrix whose entries are defined by

$$\tilde{S}_{jj'} = \delta_{jj'} + \sum_{i=1}^n \left(\frac{\partial P_{ij'}}{\partial x_j} + \frac{\partial P_{ij}}{\partial x_{j'}} \right) (x^*) (x_i^* - \tilde{x}_i) + \frac{1}{2} \sum_{k,l} \frac{\partial^2 P_{kl}(x^*)}{\partial x_j \partial x_{j'}} (x_k^* - \tilde{x}_k) (x_l^* - \tilde{x}_l), \quad (56)$$

for $1 \leq j, j' \leq n$. By the Gershgorin circle theorem and the condition $\|x^* - \tilde{x}\|_\infty < \min\{1, \frac{2}{n^2(4M_1+M_2)}\}$, the matrix \tilde{S} is also positive definite. From (53)(54)(56), $p_\sigma(\tilde{x}|x)$ can be written as

$$p_\sigma(\tilde{x}|x) = (2\pi)^{-\frac{n}{2}} \sigma^{-d} (\sigma^{-\alpha})^{n-d} (1 + o(1)) e^{-\frac{1}{2\sigma^2} v^T \tilde{S} v - \frac{1}{\sigma^{2\alpha}} |x^* - \tilde{x}|^2 + \frac{1}{\sigma^2} O(|v|^3) + \frac{1}{\sigma^{2\alpha}} O(|v|^2)}. \quad (57)$$

Noting that $(x - \tilde{x})^T \Sigma_\sigma(x)^{-1} (x - \tilde{x}) \geq \frac{1}{1 + \sigma^{2-2\alpha}} \frac{1}{\sigma^{2\alpha}} |x - \tilde{x}|^2$, there exists $\delta > 0$ such that $(x - \tilde{x})^T \Sigma_\sigma(x)^{-1} (x - \tilde{x}) - \frac{1}{\sigma^{2\alpha}} |x^* - \tilde{x}|^2 \geq \frac{\delta}{\sigma^{2\alpha}}$ for all $x \in \mathcal{M} \setminus \mathcal{O}'$, where $\mathcal{O}' := \exp_{x^*}(\mathcal{O})$. For any $m \in \mathbb{R}$, we have

$$\begin{aligned}
& \sigma^m \int_{\mathcal{M}} |x - x^*| p_0(x) p_\sigma(\tilde{x}|x) d\sigma_{\mathcal{M}}(x) \\
& \leq \sigma^m \int_{\mathcal{M}} (2\pi)^{-\frac{n}{2}} |\det \Sigma_\sigma(x)|^{-\frac{1}{2}} |x - x^*| p_0(x) d\sigma_{\mathcal{M}}(x) e^{-\frac{1}{\sigma^{2\alpha}} |x^* - \tilde{x}|^2 - \frac{\delta}{\sigma^{2\alpha}}} \\
& \leq e^{-\frac{1}{\sigma^{2\alpha}} |x^* - \tilde{x}|^2} o(e^{-\frac{\delta}{4\sigma^\alpha}}).
\end{aligned} \tag{58}$$

Similarly, the order of $-\Sigma_\sigma(x)^{-1}(\tilde{x} - x)$ can be estimated as

$$\begin{aligned}
& -\Sigma_\sigma(x)^{-1}(\tilde{x} - x) \\
& = \frac{1}{\sigma^2} P(x)(x - \tilde{x}) + \frac{1}{\sigma^{2\alpha}} \frac{1}{1 + \sigma^{2-2\alpha}} (I - P(x))(x - \tilde{x}) \\
& = \frac{1}{\sigma^2} (P(x^*) + \sum_k \frac{\partial P}{\partial x_k}(x^*) v_k + O(|v|^2))(x^* - \tilde{x} + v + O(|v|^2)) \\
& \quad + \frac{1}{\sigma^{2\alpha}} \frac{1}{1 + \sigma^{2-2\alpha}} (I - P(x^*) - \sum_k \frac{\partial P}{\partial x_k}(x^*) v_k + O(|v|^2))(x^* - \tilde{x} + v + O(|v|^2)) \\
& = \frac{1}{\sigma^2} (v + H v + O(|v|^2)) + \frac{1}{\sigma^{2\alpha}} \frac{1}{1 + \sigma^{2-2\alpha}} (x^* - \tilde{x} - H v) + \frac{1}{\sigma^{2\alpha}} O(|v|^2),
\end{aligned} \tag{59}$$

where we denote $H \in \mathbb{R}^{n \times n}$ with $H_{ij} = \sum_l \frac{\partial P_{il}}{\partial x_j}(\tilde{x})(x_l^* - x_l)$. Therefore,

$$\begin{aligned}
& \nabla_{\tilde{x}} p_\sigma(\tilde{x}) - \frac{x^* - \tilde{x}}{\sigma^{2\alpha}} \frac{1}{1 + \sigma^{2-2\alpha}} p_\sigma(\tilde{x}) \\
& = \int_{\mathcal{M}} p_0(x) \left(-\Sigma_\sigma(x)^{-1}(\tilde{x} - x) - \frac{x^* - \tilde{x}}{\sigma^{2\alpha}} \frac{1}{1 + \sigma^{2-2\alpha}} \right) p_\sigma(\tilde{x}|x) d\sigma_{\mathcal{M}}(x) \\
& = \int_{\mathcal{O}} p_0(x) \left(\frac{1}{\sigma^2} (v + H v + O(|v|^2)) - \frac{1}{\sigma^{2\alpha}} \frac{1}{1 + \sigma^{2-2\alpha}} H v + \frac{1}{\sigma^{2\alpha}} O(|v|^2) \right) p_\sigma(\tilde{x}|x) d\sigma_{\mathcal{M}}(x) \\
& \quad + e^{-\frac{1}{\sigma^{2\alpha}} |x^* - \tilde{x}|^2} o(e^{-\frac{\delta}{4\sigma^\alpha}}) \\
& = \int_{\mathcal{O}} \sigma^{-d} \left(p_0(x^*) + O(|v|) \right) \left(\frac{1}{\sigma^2} (v + H v + O(|v|^2)) - \frac{1}{\sigma^{2\alpha}} \frac{1}{1 + \sigma^{2-2\alpha}} H v + \frac{1}{\sigma^{2\alpha}} O(|v|^2) \right) \\
& \quad \cdot e^{-\frac{1}{\sigma^2} v^T \tilde{S} v + \frac{1}{\sigma^2} O(|v|^3) + \frac{1}{\sigma^{2\alpha}} O(|v|^2)} dv \cdot (2\pi)^{-\frac{n}{2}} (\sigma^{-\alpha})^{n-d} e^{-\frac{1}{\sigma^{2\alpha}} |x^* - \tilde{x}|^2} (1 + o(1)) \\
& \quad + e^{-\frac{1}{\sigma^{2\alpha}} |x^* - \tilde{x}|^2} o(e^{-\frac{\delta}{4\sigma^\alpha}}) \\
& = \int_{\mathcal{O}_\sigma} \left(p_0(x^*) + O(\sigma) \right) \left(\frac{1}{\sigma} (I + H) v' - \frac{\sigma^{1-2\alpha}}{1 + \sigma^{2-2\alpha}} H v' + O(1) \right) e^{-v'^T S_1 v' + O(\sigma) + O(\sigma^{2-2\alpha})} dv' \\
& \quad \cdot (2\pi)^{-\frac{n}{2}} (\sigma^{-\alpha})^{n-d} e^{-\frac{1}{\sigma^{2\alpha}} |x^* - \tilde{x}|^2} + e^{-\frac{1}{\sigma^{2\alpha}} |x^* - \tilde{x}|^2} o(e^{-\frac{\delta}{4\sigma^\alpha}}) \\
& = (\sigma^{-\alpha})^{n-d} e^{-\frac{1}{\sigma^{2\alpha}} |x^* - \tilde{x}|^2} O(\sigma^{(1-2\alpha) \wedge 0}),
\end{aligned} \tag{60}$$

where the third equality follows from a change of variables by $v = \sigma v'$ and $\mathcal{O}_\sigma := \{\sigma^{-1} v | v \in \mathcal{O}\}$, and $O(\sigma) + O(\sigma^{2-2\alpha}) = O(\sigma^{(2-2\alpha) \wedge 1})$. Besides, using a similar derivation, we can obtain the expansion for p_σ ,

$$p_\sigma(\tilde{x}) = (\sigma^{-\alpha})^{n-d} e^{-\frac{1}{\sigma^{2\alpha}} |x^* - \tilde{x}|^2} (p_0(x^*) + O(\sigma)). \tag{61}$$

The first claim is obtained by combining (60) and (61).

Proof of the second claim. Now we consider the case where $\tilde{x} \in \mathcal{M}$. In this case, $\tilde{x} = x^*$. By the change of variables $x = \exp_{x^*}(v)$, the quadratic form becomes $(x - \tilde{x})^T \Sigma_\sigma(x)^{-1} (x - \tilde{x}) = \frac{1}{\sigma^2} (|v|^2 + O(|v|^3)) + \frac{1}{\sigma^{2\alpha}} O(|v|^4)$. Similar to (41) and (46), we aim to show that

$$\begin{aligned}
& \nabla_{\tilde{x}} p_{\sigma}(\tilde{x}) - \int_{\mathcal{M}} \nabla_x^{\mathcal{M}} p_0(x) p_{\sigma}(\tilde{x}|x) d\sigma_{\mathcal{M}}(x) \\
& = (2\pi\sigma^{2\alpha})^{\frac{d-n}{2}} p_0(\tilde{x}) \left[-\frac{1}{2} \sum_{j,j'=1}^n \nabla_{\tilde{x}} P_{jj'}(\tilde{x}) P_{jj'}(\tilde{x}) + O(\sigma^{1\wedge(2-2\alpha)}) \right].
\end{aligned} \tag{62}$$

First, by integration by parts,

$$\begin{aligned}
& \nabla_{\tilde{x}} p_{\sigma}(\tilde{x}) - \int_{\mathcal{M}} \nabla_x^{\mathcal{M}} p_0(x) p_{\sigma}(\tilde{x}|x) d\sigma_{\mathcal{M}}(x) \\
& = \int_{\mathcal{M}} p_0(x) (\nabla_{\tilde{x}} p_{\sigma}(\tilde{x}|x) + \nabla_x^{\mathcal{M}} p_{\sigma}(\tilde{x}|x)) d\sigma_{\mathcal{M}}(x) \\
& = \int_{\mathcal{M}} p_0(x) \left[(I - P(x)) \Sigma_{\sigma}(x)^{-1} (x - \tilde{x}) - \frac{1}{2} \sum_{i,j,k} (x_i - \tilde{x}_i) P_{.k} \frac{\partial(\Sigma_{\sigma}^{ij})^{-1}}{\partial x_k}(x) (x_j - \tilde{x}_j) \right] \\
& \quad \cdot p_{\sigma}(\tilde{x}|x) d\sigma_{\mathcal{M}}(x).
\end{aligned} \tag{63}$$

From (50), we have

$$(I - P(x)) \Sigma_{\sigma}(x)^{-1} (x - \tilde{x}) = \frac{1}{\sigma^{2\alpha}} \frac{1}{1 + \sigma^{2-2\alpha}} (I - P(x)) (x - \tilde{x}) = \frac{1}{\sigma^{2\alpha}} O(|v|^2) \tag{64}$$

$$\begin{aligned}
& \frac{1}{2} \sum_{i,j,k} (x_i - \tilde{x}_i) P_{.k} \frac{\partial}{\partial x_k} (\Sigma_{\sigma}^{ij})^{-1}(x) (x_j - \tilde{x}_j) \\
& = \frac{1}{2\sigma^2} \sum_{i,j,k} (x_i - \tilde{x}_i) P_{.k} \frac{\partial}{\partial x_k} P_{ij}(x) (x_j - \tilde{x}_j) + \frac{1}{\sigma^{2\alpha}} O(|v|^2) \\
& = \frac{1}{2\sigma^2} \sum_{i,j,k} P_{.k} \frac{\partial P_{ij}}{\partial x_k}(\tilde{x}) v_i v_j + \frac{1}{2\sigma^2} O(|v|^3) + \frac{1}{\sigma^{2\alpha}} O(|v|^2).
\end{aligned} \tag{65}$$

Next, we continue to calculate (63) using (64) (65). There exists $\delta > 0$ and \mathcal{O}' such that

$$(x - \tilde{x})^T \Sigma_{\sigma}(x)^{-1} (x - \tilde{x}) \geq \frac{1}{2\sigma^{2\alpha}} \frac{|x - \tilde{x}|^2}{1 + \sigma^{2-2\alpha}} > \frac{\delta}{\sigma^{2\alpha}}, \quad \forall \sigma > 0, \quad x \in \mathcal{M} \setminus \mathcal{O}'. \tag{66}$$

Therefore, the value of the integral (63) in $x \in \mathcal{M} \setminus \mathcal{O}'$ is $o(e^{-\frac{\delta}{4\sigma^{\alpha}}})$. Using the same derivation as in (46), we have

$$\begin{aligned}
& \nabla_{\tilde{x}} p_{\sigma}(\tilde{x}) - \int_{\mathcal{M}} \nabla_x^{\mathcal{M}} p_0(x) p_{\sigma}(\tilde{x}|x) d\sigma_{\mathcal{M}}(x) \\
& = \int_{\mathcal{O}'} p_0(\tilde{x} + O(|v|)) \left(-\frac{1}{2\sigma^2} \sum_{i,j,k} P_{.k} \frac{\partial P_{ij}}{\partial x_k}(\tilde{x}) v_i v_j + \frac{1}{2\sigma^2} O(|v|^3) + \frac{1}{\sigma^{2\alpha}} O(|v|^2) \right) \\
& \quad \cdot p_{\sigma}(\tilde{x} | \exp_{x^*}(v)) dv + o(e^{-\frac{\delta}{4\sigma^{\alpha}}}) \\
& = (2\pi\sigma^{2\alpha})^{\frac{d-n}{2}} p_0(\tilde{x}) \left[-\frac{1}{2} \sum_{k,j,j'} P_{.k} \frac{\partial P_{jj'}}{\partial x_k}(\tilde{x}) P_{jj'}(\tilde{x}) + O(\sigma^{1\wedge(2-2\alpha)}) \right] + o(e^{-\frac{\delta}{4\sigma^{\alpha}}}).
\end{aligned} \tag{67}$$

Therefore, (62) holds. Besides,

$$\begin{aligned} \sum_{j,j'=1}^n \nabla P_{jj'} P_{jj'} &= \sum_{k,j,j'=1}^n \nabla (P_{jk} P_{kj'}) P_{jj'} = \sum_{k,j,j'=1}^n \nabla (P_{kj'}) P_{jk} P_{jj'} + \sum_{k,j,j'=1}^n \nabla (P_{jk}) P_{kj'} P_{jj'} \\ &= 2 \sum_{j,j'=1}^n \nabla P_{jj'} P_{jj'}. \end{aligned} \quad (68)$$

implies $\sum_{j,j'=1}^n \nabla P_{jj'}(\tilde{x}) P_{jj'}(\tilde{x}) = 0$. Therefore, (62) becomes

$$\nabla_{\tilde{x}} p_{\sigma}(\tilde{x}) - \int_{\mathcal{M}} \nabla_x^{\mathcal{M}} p_0(x) p_{\sigma}(\tilde{x}|x) d\sigma_{\mathcal{M}}(x) = (2\pi\sigma^{2\alpha})^{\frac{d-n}{2}} p_0(\tilde{x}) O(\sigma^{1\wedge(2-2\alpha)}). \quad (69)$$

Similarly, we have

$$\int_{\mathcal{M}} \nabla_x^{\mathcal{M}} p_0(x) p_{\sigma}(\tilde{x}|x) d\sigma_{\mathcal{M}}(x) = (2\pi\sigma^{2\alpha})^{\frac{d-n}{2}} \left(\nabla_{\tilde{x}}^{\mathcal{M}} p_0(\tilde{x}) + O(\sigma^{(2-2\alpha)\wedge 1}) \right), \quad (70)$$

$$p_{\sigma}(\tilde{x}) = \int_{\mathcal{M}} p_0(x) p_{\sigma}(\tilde{x}|x) d\sigma_{\mathcal{M}}(x) = (2\pi\sigma^{2\alpha})^{\frac{d-n}{2}} \left(p_0(\tilde{x}) + O(\sigma^{(2-2\alpha)\wedge 1}) \right). \quad (71)$$

Using (69) (70) (71), the second claim is obtained via

$$\nabla_{\tilde{x}} \log p_{\sigma}(\tilde{x}) = \frac{\nabla_{\tilde{x}} p_{\sigma}(\tilde{x})}{p_{\sigma}(\tilde{x})} = \nabla_{\tilde{x}}^{\mathcal{M}} \log p_0(\tilde{x}) + O(\sigma^{1\wedge(2-2\alpha)}). \quad (72)$$

C Algorithm details

C.1 Details of the Tango loss

We first prove the validity of the loss (20). Note that

$$\begin{aligned} &\mathbb{E}_{x_t} \|s_{\theta}^{\parallel}(x_t, t) - P(x_t) \nabla_{x_t} \log p_{\sigma_t}(x_t)\|^2 \\ &= \mathbb{E}_{x_t} \|P(x_t) s_{\theta}(x_t, t)\|^2 - \mathbb{E}_{x_t} \langle P(x_t) s_{\theta}(x_t, t), P(x_t) \nabla_{x_t} \log p_{\sigma_t}(x_t) \rangle + C \\ &= \mathbb{E}_{x_t} \|P(x_t) s_{\theta}(x_t, t)\|^2 - \int \langle P(x_t) s_{\theta}(x_t, t), \nabla_{x_t} p_{\sigma_t}(x_t) \rangle dx_t + C \\ &= \mathbb{E}_{x_t} \|P(x_t) s_{\theta}(x_t, t)\|^2 - \mathbb{E}_x \left\langle P(x_t) s_{\theta}(x_t, t), \nabla_{x_t} \int p_{\sigma_t}(x_t|x) p_0(x) dx \right\rangle dx_t + C \\ &= \mathbb{E}_{x_t} \|P(x_t) s_{\theta}(x_t, t)\|^2 - \int \int \langle P(x_t) s_{\theta}(x_t, t), \nabla_{x_t} \log p_{\sigma_t}(x_t|x) \rangle p_{\sigma_t}(x_t|x) p_0(x) dx dx_t + C \\ &= \mathbb{E}_{x_t} \|P(x_t) s_{\theta}(x_t, t)\|^2 - \mathbb{E}_{x, x_t} \langle P(x_t) s_{\theta}(x_t, t), \nabla_{x_t} \log p_{\sigma_t}(x_t|x) \rangle + C \\ &= \mathbb{E}_{x, x_t} \|s_{\theta}^{\parallel}(x_t, t) - P(x_t) \nabla_{x_t} \log p_{\sigma_t}(x_t|x)\|^2 + C_1. \end{aligned} \quad (73)$$

Therefore,

$$\arg \min_{s_{\theta}^{\parallel}} \mathbb{E}_{x, x_t} \|s_{\theta}^{\parallel}(x_t, t) - P(x_t) \nabla_{x_t} \log p_{\sigma_t}(x_t|x)\|^2 = P(x_t) \nabla_{x_t} \log p_{\sigma_t}(x_t). \quad (74)$$

The overall loss calculation is summarized in Algorithm 1.

C.2 Details of the sampling algorithm

Algorithms 2 and 3 provide detailed descriptions of the Reverse SDE and the Annealing SDE on manifolds, respectively. The threshold $\bar{\sigma}$ in Algorithm 3 is set to c_{niso} and c_{tango} for Niso-DM and Tango-DM, respectively.

D Experiment details

Algorithm 1 The overall loss calculation with the Tango loss

Require: neural network s_θ , threshold c_{tango}

- 1: Sample $t \sim \mathcal{U}(0, 1)$, $x \sim p_0$
 - 2: **if** $\sigma_t \geq c_{\text{tango}}$ **then**
 - 3: Calculate loss: $\lambda_t \mathbb{E}_{x, x_t} \|s_\theta(x_t, t) - \nabla_{x_t} \log p_{\sigma_t}(x_t|x)\|^2$
 - 4: **else**
 - 5: Calculate loss: $\lambda_t \mathbb{E}_{x, x_t} \|P(x_t)s_\theta(x_t, t) - P(x_t)\nabla_{x_t} \log p_{\sigma_t}(x_t|x)\|^2$
 - 6: **end if**
-

Algorithm 2 Reverse SDE Solver

Require: trained neural network s_θ , total number of discrete SDE steps N , projection operator π

- 1: $t \leftarrow T$, $\Delta t > 0 = T/N$
 - 2: $x_t \sim \mathcal{N}(0, \sigma_{\text{max}}^2 I)$
 - 3: **while** $t > 0$ **do**
 - 4: $z \sim \mathcal{N}(0, I)$
 - 5: $x_t \leftarrow x_t + g(t)^2 s_\theta(x_t, t) \Delta t + g(t) \sqrt{\Delta t} z$
 - 6: $t \leftarrow t - \Delta t$
 - 7: **end while**
 - 8: *%Projection onto the manifold*
 - 9: $x_t \leftarrow \pi(x_t)$
 - 10: **return** x_t
-

Algorithm 3 Annealing SDE on manifolds

Require: Trained neural network s_θ , total number of discrete SDE steps N , threshold $\tilde{\sigma}$, number of steps n_0 and step size α_{1d} for the Langevin dynamics on manifolds, projection operator π

- 1: $t \leftarrow T$, $\Delta t > 0 = T/N$, $x_t \sim \mathcal{N}(0, \sigma_{\text{max}}^2 I)$
 - 2: *%Stage 1: Reverse SDE*
 - 3: **while** $\sigma_t \geq \tilde{\sigma}$ **do**
 - 4: $z \sim \mathcal{N}(0, I)$
 - 5: $x_t \leftarrow x_t + g(t)^2 s_\theta(x_t, t) \Delta t + g(t) \sqrt{\Delta t} z$
 - 6: $t \leftarrow t - \Delta t$
 - 7: **end while**
 - 8: *%Stage 2: Annealing SDE on manifolds*
 - 9: $x_t \leftarrow \pi(x_t)$
 - 10: **while** $t > 0$ **do**
 - 11: **for** $i = 0$ to n_0 **do**
 - 12: $z \sim \mathcal{N}(0, I)$, $z_1 \leftarrow P(x)z$
 - 13: $x'_t \leftarrow x_t + \alpha_{1d} P(x_t) s_\theta(x_t, t) + \sqrt{2\alpha_{1d}} z_1$
 - 14: $x_t \leftarrow \pi(x'_t)$
 - 15: **end for**
 - 16: $t \leftarrow t - \Delta t$
 - 17: **end while**
 - 18: **return** x_t
-

The details of each experiment are provided in the subsections below. The neural network used is a multilayer perceptron (MLP) with SiLU as the activation function. Models are trained using PyTorch, utilizing the Adam optimizer with a fixed learning rate and gradients are clipped when their 2-norm exceeds a predefined threshold. An exponential moving average of the model weights [24] is applied with a decay rate of 0.999. In each run, the dataset is divided into training and test sets with ratio 8 : 2. All experiments are conducted on either a single Tesla V100-PCIE-32GB GPU or an NVIDIA A40 GPU with 48GB of memory. The values of all parameters used in the experiments are listed in Table 5.

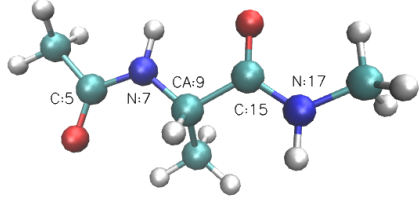


Figure 2: Illustration of the Alanine dipeptide system: The dihedral angles ϕ and ψ are defined by atoms whose indices are 5, 7, 9, 15 and 7, 9, 15, 17, respectively. This figure is from [17].

When the rescaling technique is not applied, the time reweighting coefficient λ_t is defined as σ_t^2 . In contrast, when the rescaling technique is applied, λ_t is defined as $\sigma_t w_t$, where w_t represents the scaling factor of the optimal score function. Specifically, w_t corresponds to σ_t in Iso-DM, $\sqrt{\sigma_t^2 + c_{\text{niso}}^2}$ in Niso-DM, and $\max\{\sigma_t, c_{\text{tango}}\}$ in Tango-DM.

Table 5: Parameters in our experiments. σ_{\min} , σ_{\max} , and T are the parameters of the SDE. c_{niso} and c_{tango} are the parameters for Niso-DM and Tango-DM, respectively. N , n_0 , and α_{ld} are the hyperparameters of the sampling algorithm. N_{epoch} , B , lr, and clip denote the total epochs, batch size, learning rate, and gradient clipping threshold during training. N_{node} and N_{layer} represent the number of hidden nodes per layer and the number of hidden layers in the neural networks, respectively. \mathcal{D} indicates the dataset size.

Parameters	Hyperplane	Bunny	Spot	SO(10)	dipeptide
σ_{\min}	0.001	0.001	0.001	0.0005	0.0001
σ_{\max}	3	3	3	3	5
T	1	1	1	1	1
c_{niso}	0.2	0.002	0.002	0.01	0.005
c_{tango}	0.2	0.002	0.002	0.05	0.005
N	500	200	200	500	500
n_0	10	20	10	10	10
α_{ld}	0.01	0.05	0.05	0.05	0.05
N_{node}	64	256	256	512	512
N_{layer}	3	3	3	3	5
N_{epoch}	200	20000	20000	5000	6000
B	512	4096	4096	512	1024
lr	0.0005	0.0005	0.0005	0.001	0.0005
clip	10	10	10	1	10
\mathcal{D}	50000	60000	60000	50000	99999

D.1 The hyperplane in 3D space

The target distribution is a mixture of Gaussian distributions with nine modes located on the plane. Specifically, the means of the nine modes are $(-1, -1)$, $(-1, 0)$, $(-1, 1)$, $(0, -1)$, $(0, 0)$, $(0, 1)$, $(1, -1)$, $(1, 0)$, and $(1, 1)$, and each Gaussian has a standard deviation of 0.3.

D.2 Mesh data

To create the datasets, we first obtain the clamped eigenfunction of the Laplacian operator on a mesh that has been upsampled threefold for the original mesh. The target distribution is chosen as an equal-proportion mixture of density functions corresponding to the 0-th, 500-th, and 1000-th eigenpairs. For the distribution on the cow mesh, we additionally discarded the points on the horns and tail.

D.3 High-dimensional special orthogonal group

The manifold $SO(10)$ is defined as $\{Q \in \mathbb{R}^{10 \times 10} | QQ^T = I_{10}, \det(Q) = 1\}$, which represents (a connected component of) the zero-level set of the map $\xi : \mathbb{R}^{100} \rightarrow \mathbb{R}^{55}$. The components of ξ correspond to the upper triangular portion of the matrix $Q^T Q - I_{10}$. The dataset is constructed as a mixture of 5 wrapped normal distributions. Each wrapped normal distribution is the image (under the exponential map) of a normal distribution defined in the tangent space at a pre-selected center. For more details, refer to [17].

D.4 Alanine dipeptide

To generate the dataset, we follow [17] to obtain the target distribution on the manifold $\mathcal{M} = \{x \in \mathbb{R}^{30} | \phi(x) = -70^\circ\}$. We also ensure that the generated distribution is $SE(3)$ -invariant (i.e., invariant under rotations and translations) by incorporating alignment before feeding the data into the neural network.

E Bias-variance tradeoff

Recall that the noise scale σ_t is chosen as $\sigma_t = \sigma_{\min}(\sigma_{\max}/\sigma_{\min})^{t/T}$ and $0 < \sigma_{\min} \ll 1$. When t is sufficiently small, σ_t approaches σ_{\min} , and the singularity of the score function primarily depends on σ_{\min} . As σ_{\min} decreases, the singularity becomes pronounced.

For Iso-DM, there exists a bias-variance trade-off in the choice of σ_{\min} . A very small σ_{\min} reduces bias but increases variance, resulting in a larger overall error. In this case, $\nabla_x \log p_{\sigma_{\min}}(x)$ approximates $\nabla_x \log p_0(x)$ well; however, severe multiscale discrepancies between its tangential and normal components hinder learning. Conversely, a very large σ_{\min} increases bias and reduces variance, yet the overall error still increases. In this scenario, $\nabla_x \log p_{\sigma_{\min}}(x)$ fails to serve as a good approximation of $\nabla_x \log p_0(x)$, although the singularity issue is less pronounced. Figure 3a illustrates this phenomenon, where the red line represents the error for Iso-DM.

For Niso-DM, the singularity is governed by the additional noise scale c_{niso} for Niso-DM, rather than σ_{\min} . As a result, our method exhibits greater robustness as σ_{\min} decreases. The blue line in Figure 3a demonstrates the stability of the error for Niso-DM under varying σ_{\min} .

Figures 3b and 3c show the impact of c_{niso} in Niso-DM and c_{tango} in Tango-DM on the error. The selection of these hyperparameters also involves a bias-variance trade-off.

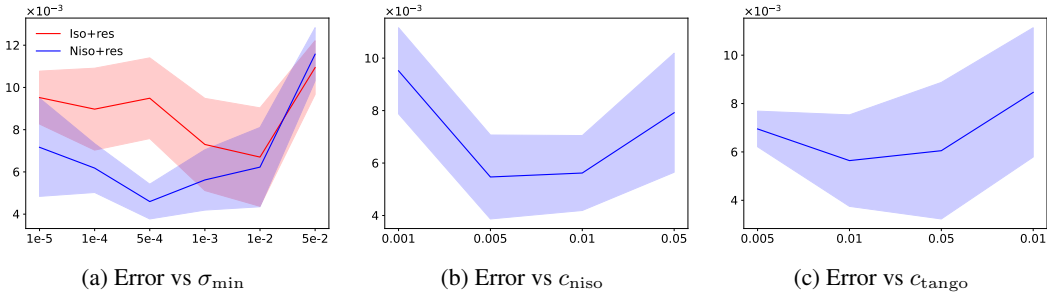


Figure 3: Ablation Studies for $SO(10)$: The solid line denotes the mean, while the shaded area indicates the standard deviation. (a) The error of the distribution generated by the Reverse SDE algorithm under the Iso-DM (red) and Niso-DM (blue) methods with varying σ_{\min} . (b) The impact of c_{niso} on the error with $\sigma_{\min} = 0.001$. (c) The impact of c_{tango} on the error with $\sigma_{\min} = 0.001$.